



ORIGINAL RESEARCH ARTICLE

# Effect of Layer Thickness in Cold Metal Transfer Cladding of Fe-Based ER70S-6 Alloy on AA 6061-T6 Aluminum Alloy

Bappa Das, Biranchi N. Panda, and Uday S. Dixit

Submitted: 8 August 2023 / Revised: 30 January 2024 / Accepted: 22 April 2024

This study explores the effectiveness of the cold metal transfer (CMT) technique in producing thick cladding without significantly heating substrate materials. Fe-based alloy cladding with thicknesses of 1, 2, and 3 mm were obtained by deposition on AA 6061-T6 alloy and post-machining. The dilution, bead contact angle and surface roughness were the least in 1 mm thick cladding layer due to enhanced cooling rate. In the 1 mm thick cladding layer, the grain size was relatively small with an average size of 40  $\mu\text{m}$ . The porosity, microhardness, Lancaster wear coefficient and shear bond strength were 1.75%, 282 HV,  $0.88 \times 10^{-5} \text{ mm}^3/\text{N m}$  and 88 MPa, respectively. The corresponding values were 2.69%, 249 HV,  $1.03 \times 10^{-5} \text{ mm}^3/\text{N m}$  and 77 MPa for 3 mm thick cladding. Improved properties of 1 mm thick cladding are attributed to enhanced low angle grain boundaries, higher dislocation density and dense martensitic structure. However, tripling the cladding layer thickness from 1 to 3 mm does not deteriorate the properties in that proportion. Hence, in applications like additive manufacturing, an optimum layer thickness can be chosen for providing the best trade-off between properties and production rate.

**Keywords** aluminum alloy, cladding, CMT process, hardness, microstructure, wear

## 1. Introduction

One of the important guiding principles of sustainable engineering is the minimization of the depletion of resources. By minimizing the consumption of material in a product, a designer also saves the energy in manufacturing and operating the products. At the end of its lifecycle, a lighter product generates lesser waste than that generated by a heavier product. For optimum utilization of the material, often high strength steel and lightweight aluminum (Al) alloys are combined in a judicious way to make a composite structure. It is common to see such type of composite structures in automobiles, airplanes and ships. However, the different material properties of Al and steel make their joining a challenging task. Difference in melting temperatures, heat conductivities and coefficients of thermal expansion of these materials produces residual stresses and many other defects. For joining Al to steel, a variety of welding techniques such as laser beam welding, gas metal arc welding (GMAW), and friction stir welding are used, but quality of joint is poor in the most of the cases (Ref 1, 2). The mechanical characteristics of the finished product are impacted due to the fast oxidation of weld metal and subsequent

development of a brittle intermetallic layer. To overcome the problems a few researchers used cold metal transfer (CMT) welding technique to joint Al and steel (Ref 3).

Fundamentally, CMT technique operates in a short-circuit mode with low current and voltage, which generates very low heat input during the process (Ref 4, 5). The metal transfer takes place with an extremely low current and the length of the arc is very small. With the support of complete computer control, CMT produces a spatter-free and smoother weld bead than that produced in GMAW (Ref 6). Selvi et al. (Ref 3) outlined the working principle, tools, application and restrictions of CMT. With less heat input during the CMT process, distortion and residual stresses are also reduced in addition to the superior weld bead quality.

Aluminum (Al) and its alloys possess high specific strength and high corrosion resistance. However, they have poor wear resistance and hardness, which could decrease the lifespan of products made of Al alloys. Surface cladding and coating of steel on aluminum can improve the lifespan of products. Weld overlay is frequently used to join materials, but it is also popular for mending damaged parts.

Several studies have investigated the use of steel powders to coat the surface of Al to enhance its wear resistance and hardness. Sova et al. (Ref 7) employed a cold spray technique to deposit 316 L stainless steel powder onto the Al surface, but encountered a notable presence of porosity between the deposited layers. Villa et al. (Ref 8) deposited 316 L stainless powder onto the Al surface, and observed a significantly improved wear resistance at the coated surface compared to base Al surface. Zhou et al. (Ref 9) utilized high-speed particle injection to deposit 316 L stainless powder onto an Al alloy sheet at a spraying temperature of approximately 400 °C. This resulted in a coating with an enhanced hardness (HV > 400) and high wear resistance at elevated temperatures. Neverthe-

**Bappa Das, Biranchi N. Panda, and Uday S. Dixit**, Department of Mechanical Engineering, Indian Institute of Technology Guwahati, Guwahati, Assam 781039, India. Contact e-mails: uday@iitg.ac.in and usd1008@yahoo.com.

less, the thermal spray coating methods generally yield low deposition thickness in a single pass (Ref 10), and require multiple passes to achieve a thick coating. In contrast, a weld overlay process enables high deposition thickness in a single pass (Ref 11). Das et al. (Ref 12-14) cladded Fe-based ER70S-6 alloy on Al substrates. The CMT cladding of Fe-based alloy on Al substrate (Ref 12) resulted in the enhancement of mechanical properties of Al substrate. A shear bond strength of 74 MPa was measured between the cladding layer and substrate. Following a 200-h corrosion test conducted on the cladded layer and substrate, the top surface layer exhibited pitting corrosion (Ref 13). As a result, the hardness decreased by 10%, and the wear depth in the cladding layer increased by 39.5%. Different heat treatments were employed to enhance the mechanical characteristics of the deposited cladding layer (Ref 14). The most enhanced mechanical properties were obtained after the deep cryo-treatment, thanks to the refined grain and dense martensite structure. On the other hand, the wear resistance and hardness reduced after an annealing treatment (heating up to 600 °C, soaking up to an hour and then furnace cooling for a day).

Cladded layer thickness is an important decision variable. In the case of repair and reworking, it is dictated by finishing requirement. In the case of additive manufacturing, it influences total build time. When the cladding is used for the surface protection, the layer thickness has a bearing on the life of the component. However, there is hardly any article on the effect of CMT cladding layer thickness on the bonding and mechanical characteristics. The effects of coating thickness on the microstructure and mechanical characteristics of Al alloys (Ref 15-17) were studied for spray coating technology. Xiong et al. (Ref 15) observed the reduction in shear adhesive bond strength of Al 7075 and 7050 cold sprayed coatings with increasing layer thickness due to residual stress. Moridi et al. (Ref 16) also noted that thicker cold sprayed Al 6082 coatings on the similar material substrate resulted higher pores and defects. Thick coatings are typically accompanied by poor mechanical strengths in thermal spray as well (Ref 17). There is a strong need to carry out similar study for CMT cladding.

This work investigates CMT cladding of Fe-based ER70S-6 alloy on Al substrates with particular focus on the effect of cladding thickness. The choice of AA6061-T6 as the substrate and Fe-based ER70S-6 as the cladding material is based on the need to produce a tough high specific strength material with high corrosion and wear resistant surface. AA6061-T6 has high specific strength and corrosion resistance; it is used for making the frames of automobiles, rail coaches and ships. Fe-based ER70S-6 as the cladding material has exceptional welding characteristics (Ref 18) including stable arc, low sputter, cost-effectiveness, and high deposition efficiency. The presence of deoxidizers like Si and Mn in ER70S-6 enhances wetting and facilitates faster welding travel speeds, contributing to heightened productivity and extended consumable life (Ref 19). It is easily available in the form of wires and rods and is frequently used in (CMT) technique. Its capacity to form a dense martensitic structure makes it particularly well-suited for cladding applications where wear resistance is of utmost importance (Ref 20). A survey of the existing literature indicates that, while there have been studies examining the application of CMT for cladding, there is an absence of reported research specifically focusing on the effect of steel cladded thickness on aluminum alloy. While aluminum alloys have been coated with metallic powders using spray tech-

niques, a lot of porosity is obtained. Moreover, metallic powders are costly. In view of these observations, this study is undertaken to explore the utilization of CMT for cladding AA6061-T6 with ER70S-6 alloy in the form of a welding electrode with the main focus on the effect of cladded layer thickness. Choosing a proper layer thickness is also an important aspect of directed energy deposition based additive manufacturing. The properties investigated are bead contact angle, dilution, porosity level, hardness, wear and interfacial bond strength.

## 2. Experimental Details

This section provides the details of the experimental procedures as well as a characterization of the materials utilized to produce the cladded layer.

### 2.1 CMT Cladding with ER70S-6 Alloy

AA 6061-T6 alloy was used as a substrate material. Samples of size 180 mm × 100 mm × 6 mm were properly cleaned with acetone and preheated to 400 °C in an electric furnace prior to cladding process. The composition of the substrate was 0.1% Ti, 0.3% Fe, 0.3% Zn, 0.7% Si, 0.7% Cu, 0.7% Cr, 1% Mg by weight and the rest Al (Ref 12). The 1.2 mm diameter filler wire of ER70S-6 was used for cladding using a Fronius TPS400i machine. The filler rod of ER70S-6 was obtained from ESAB, India. The typical weld metal analysis as supplied by ESAB was 0.01% Al, 0.075% C, 1.45% Mn, 0.85% Si, 0.30% Cu, traces of Cr, Mo, Ni, P, S and V with balance Fe. However, in-house EDS provided Al (0.1% max.), Mn (1.4% max.) and Si (1.4% max.) on the milled cladded surface (Ref 12). The speed and path of the cladding layers were altered using the 6-axis FANUC Arc Mate 100iD robot. The experimental setup is shown in Fig. 1(a). The process parameters used during the cladding process were controlled with the attached remote-controlled unit of CMT machine. For studying the effect of cladding layer thickness, ~ 1.5, ~ 2.5 and ~ 3.5 mm cladded layer was deposited on the substrate. The cladded layers are depicted in Fig. 1(b). The thickness of ~ 0.5 mm was milled for getting a smooth surface for characterization purpose as shown in Fig. 1(c). Finally, cladded layers of 1 mm, 2 mm and 3 mm thicknesses were obtained. The extracted samples for metallurgical characterization are shown in Fig. 1(d). The process parameters are listed in Table 1. In all the cases, welding speed was kept at 6.67 mm/s. The current was varied as follows: 90 A for ~ 1.5 mm, 100 A for ~ 2.5 mm and 110 A for ~ 3.5 mm. The CMT power source includes an automatic adjustment feature for other welding parameters, including wire feed rate and arc voltage. The patterns of cladding layers are depicted in Fig. 1(c). Each cladded layer was deposited one at a time, and the next layer was deposited after a break of two minutes to allow the substrate to cool below 100 °C. The length of each layer was 140 mm. Argon was used as a shielding gas with a flow of rate of 20 l/min.

### 2.2 Microstructural and Phase Characterization

For microstructure characterization purposes the samples were sectioned through a wire cut electric discharge machine. The sectioned samples underwent polishing using SiC papers ranging from 80 to 2000 mesh grits. The diamond polishing

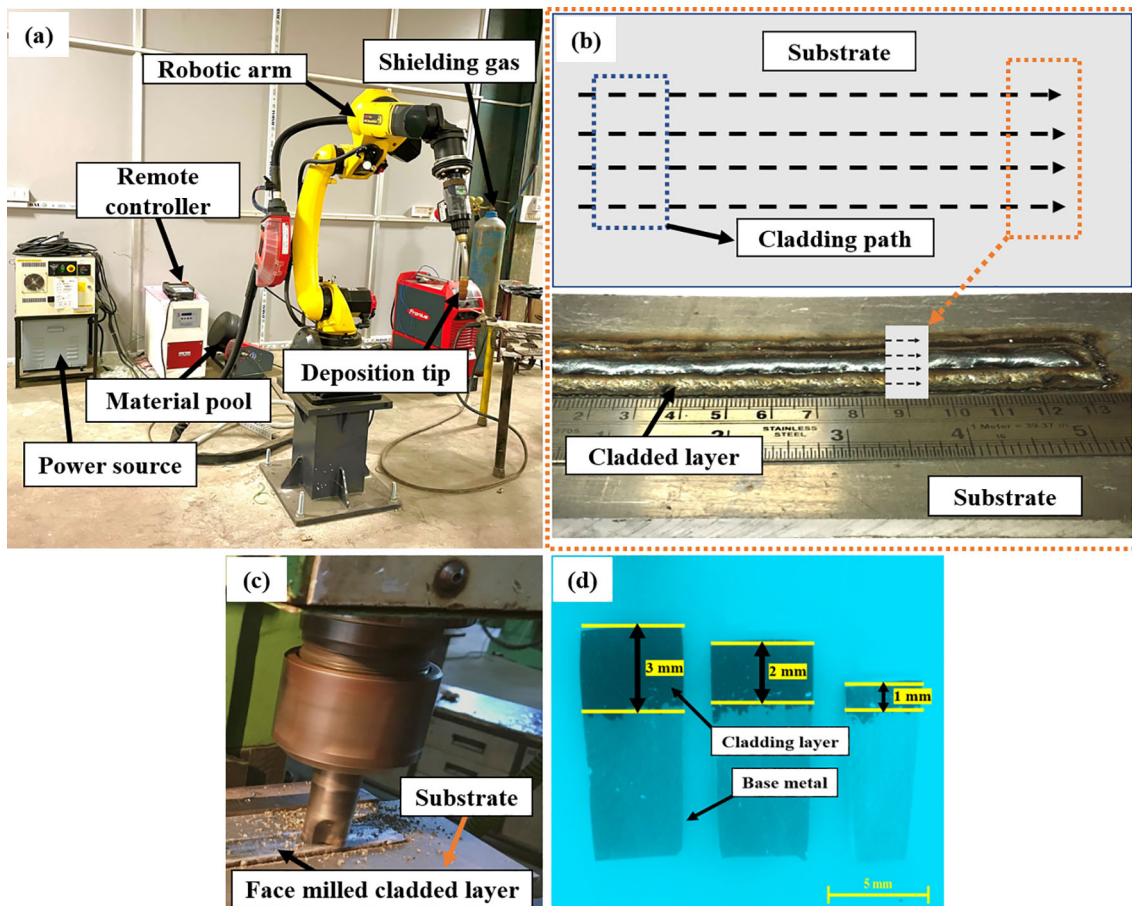


**Fig. 1** Cladding by CMT: (a) setup, (b) schematic of cladding path and deposited 3.5 mm bead, (c) face milling of sample and (c) post-machined samples of different layer thicknesses

**Table 1** CMT process parameters used during the cladding process

Cladded thickness, mm	Post-machining thickness, mm	Current, A	Voltage, V	Wire feed rate, mm/s
1.5	1	90	8	138.33
2.5	2	100	10	153.33
3.5	3	110	12	200

cloth was used to remove any scratches in the surface. In order to observe the microstructure, the polished samples were etched with Nital reagent for a duration of 15 s. The optical micrographs were obtained through upright optical microscopy (Model: Axiocam MRC; Make: Carl Zeiss). The surface roughness was measured using atomic force microscopy (AFM) (Model: Cypher S; Make: Oxford Instruments) in tapping mode. The AFM measurements were conducted on the surface of the cladded layers before surface milling. The detailed examination of grain size, grain distribution and grain misorientation was accomplished using electron backscatter diffraction (EBSD) (Model: Quanta 3D FEG; Make: FEI) without etching. Furthermore, the surface morphology of milled cladded surface was obtained through field emission electron microscopy (FESEM) (Model: Sigma 300; Make: Zeiss). The microstructural observation for different developed phases were conducted using FESEM after etching with Nital reagent. Different phases and structure were observed using

transmission electron microscopy (TEM) (Model: 2100F; Make: JEOL). The X-ray diffraction (XRD) was conducted using X-ray diffractometer machine (Model: SmartLab; Make: Rigaku) with  $\text{Cu}-\text{K}_{\alpha 1}$  radiation ( $\lambda = 1.54056$ ). The development of different compounds was analyzed using X-ray photoelectron spectroscopy (XPS) (Model: PHI 5000 Versa Probe III; Make:  $\Phi$  Ulvac-PHI, Inc.).

### 2.3 Mechanical Characterization

The porosity of the different samples was calculated according to Archimedes' principle. The detailed measurement process is reported in a related article (Ref 14). The Vickers microhardness test was conducted with 200 gf for 20 s using hardness tester (Model: MVH-II; Make: Omni Tech). The wear analysis was performed with a pin-on-disc machine (Model: TR-201, Make: Ducom). The parameters for wear test were 20 N load, 350 rpm, 70 mm track diameter, 10 mm pin diameter

and 30 min sliding time. This amounts to a sliding distance of 2309 m (Ref 14). The cladding materials in the form of pin traversed on hardened steel disc (84 HRC), according to ASTM standard: G99. The lap shear study was performed using universal testing machine (Model: 8801; Make: Instron) with an average ram speed of 0.1 mm/min, which ensured quasi-static condition (strain less of the order of  $1 \times 10^{-3}$  s $^{-1}$ ). The detailed procedure is available in a related article (Ref 12).

### 3. Results and Discussion

This section discusses the results obtained during the experimental examination. First, the bead contact angle and dilution of the obtained cladded layer is discussed. Next, the microstructure, grain size, XRD, microhardness and the results of tribological study are described. Finally, the shear lap study is discussed.

#### 3.1 Dilution and Bead Contact Angle

The dilution percentage represents the proportion of the entire bead's cross sectional area that is situated beneath the substrate's surface, as depicted in Fig. 2(a). Denoting  $A$  as the

area of the bead beneath the substrate's surface and  $B$  as the area of the bead above it. The dilution is calculated as

$$\text{Dilution}(\%) = \frac{A}{(A + B)} \times 100. \quad (\text{Eq 1})$$

The dilution increases with increasing layer thickness. As the layer thickness is increased from 1 to 3 mm, the dilution increases from 4.01 to 6.6%. The dilution for 2 mm thick bead was 5.04%. The calculated bead contact angles of different cladding layers are shown in Fig. 2(b, c and d); the reported angles are average of angles at three locations; in each case difference between the maximum and minimum contact angle is less than 3°. The bead contact angle increases from 111° to 121°, when layer thickness increases from 1 to 3 mm; it was 117° for 2 mm. Thus, the bead contact angle and dilution have positive correlation with layer thickness. A few researchers also reported the similar observation. A lower bead contact angle is desirable to avoid lack of fusion when the surface is cladded by side-by-side overlapping beads (Ref 18, 19). The 1 mm bead with contact angle 111° has provided least lack of fusion in the side-by-side (no overlapping) beads as compared to 3 mm bead with contact angle of 121°. The gap can be reduced by increasing the overlapping percentage between beads.

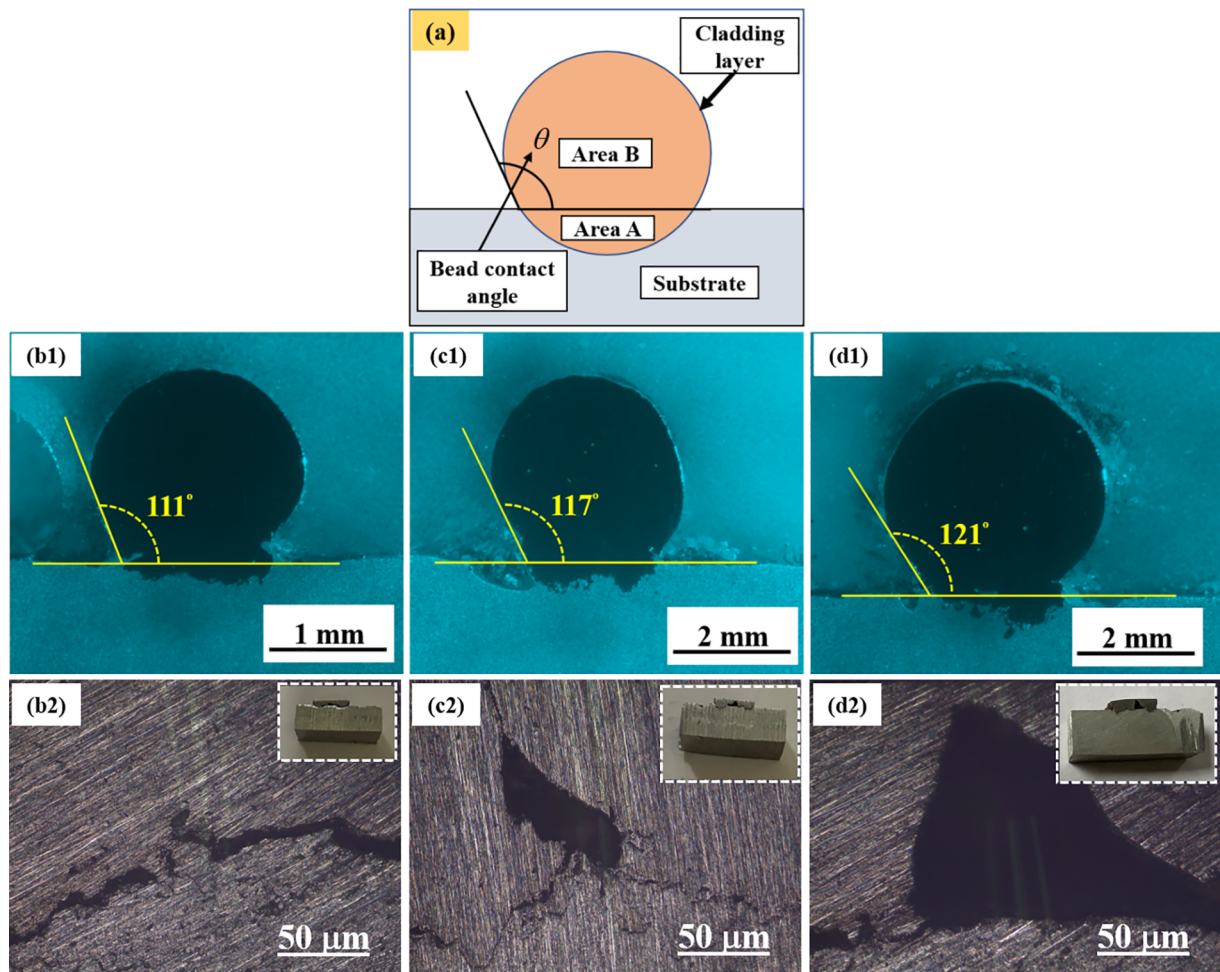


**Fig. 2** Contact angle micrograph of deposited cladding layer of different height (5x) and gap between layer to layer (10x): (a) schematic for dilution calculation, bead contact angle and gap (b1, b2) 1 mm, (c1, c2) 2 mm and (d1, d2) 3 mm

### 3.2 Cross Section and Surface Morphology

The micrographs of the cladding layer cross sections are shown in Fig. 3(a-f). None of the claddings display interface delamination or cracking. The microstructure depicts dilution of substrate by cladding material due to low melting temperature and density of the former. The positive aspect of it is a good metallurgical bonding between cladded layer and substrate. The maximum depth of cladding material into the substrate was 45 µm for the 3 mm thick cladding layer; the depth was 15 µm and 30 µm for 1 mm and 2 mm thick cladding layers, respectively. Thus, the depth of dilution of cladding material into substrate changed linearly with the layer thickness. The dilutions are related to heat input during the CMT process. The heat inputs for 1 mm, 2 mm and 3 mm cladding layer were 102.6, 142.5 J/mm and 188.1 J/mm, respectively. The heat input is calculated as

$$Q = \eta \left( \frac{VI}{S} \right), \quad (\text{Eq } 2)$$

where  $\eta = 0.95$  (Ref 23) is the efficiency,  $V$  the voltage,  $I$  the current and  $S$  is the welding speed. Fig. 3(g) shows the porosity % of three different cladding layers. The porosity was 1.75%, 2.16% and 2.69% for 1, 2 and 3 mm cladding layers, respectively.

### 3.3 Microstructure Study

**3.3.1 EBSD Observation.** The EBSD analysis was conducted on the cross section and top surface of different cladding layer thickness. The cross sectional EBSD micrographs are

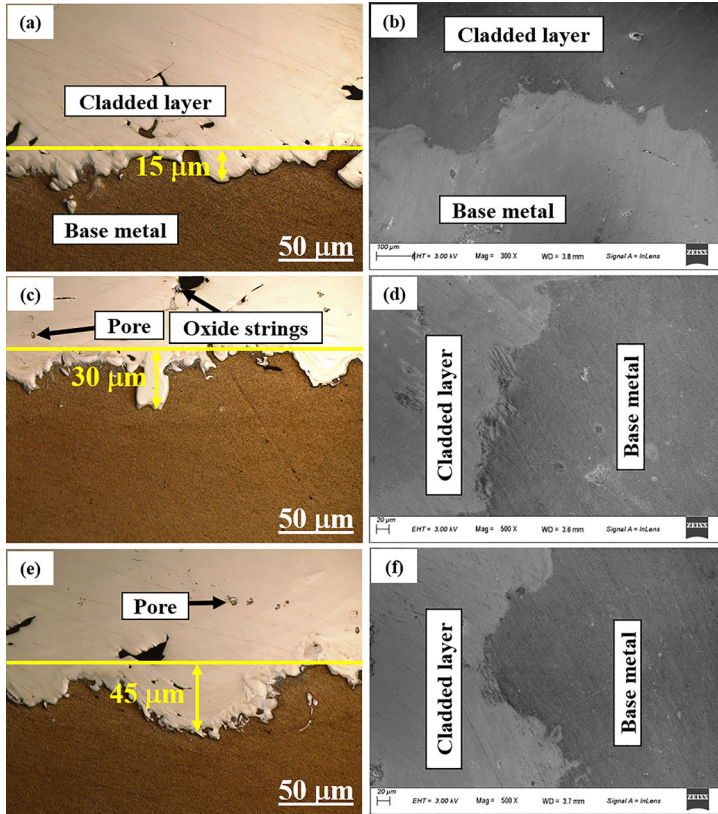


**Fig. 3** Micrographs and cross section properties of deposited cladding layer of different thicknesses: (a, b) 1 mm, (c, d) 2 mm, (e, f) 3 mm and (g) porosities

shown in Fig. 4. The analysis areas ( $1000 \times 1000 \mu\text{m}^2$ ) of cross sections are depicted in Fig. 4(a1). Fig. 4(b1, c1 and d1) show the band contrast (BC) maps of the grains near interface toward the top. In the cladding layers, the morphology of the grains changed from the bottom to the top of the layer owing to combined effect of the temperature gradient and the grain growth rate, as nicely explained by Li et al. (Ref 24) for laser cladding process. At the beginning of CMT cladding, due to the developed arc, electrode as well as substrate melted. Due to high thermal conductivity of Al alloy, the most of the heat transfer took place by conduction. The substrate served as the initial heterogeneous nucleation layer. At this point, the thermal gradient was high and grain growth rate was low; this provided high crystal nucleation speed. Therefore, nearer to the substrate in the cladding layer, some equiaxed grains were generated. After the initial formation of equiaxed grains nearer to the substrate, subsequent stages involve grain growth and directional solidification, actively promoting the development of columnar grains. Simultaneously, upward heat flow from the bottom establishes a vertical thermal gradient, playing a crucial role in achieving the desired structural characteristics in the cladding layer.

Figure 4(a2) shows the orientation along the three crystal planes of ferrite, {111}, {101}, and {001} in blue, green, and red color, respectively. Figure 4(b2, c2 and d2) show the inverse pole figure (IPF) maps of cladding layers. The different colors in IPF maps correspond to various grain orientations relative to the lattice structure. According to the color distribution in IPF maps, the grain orientations from the bottom to top (toward the building direction) is non-uniform. There

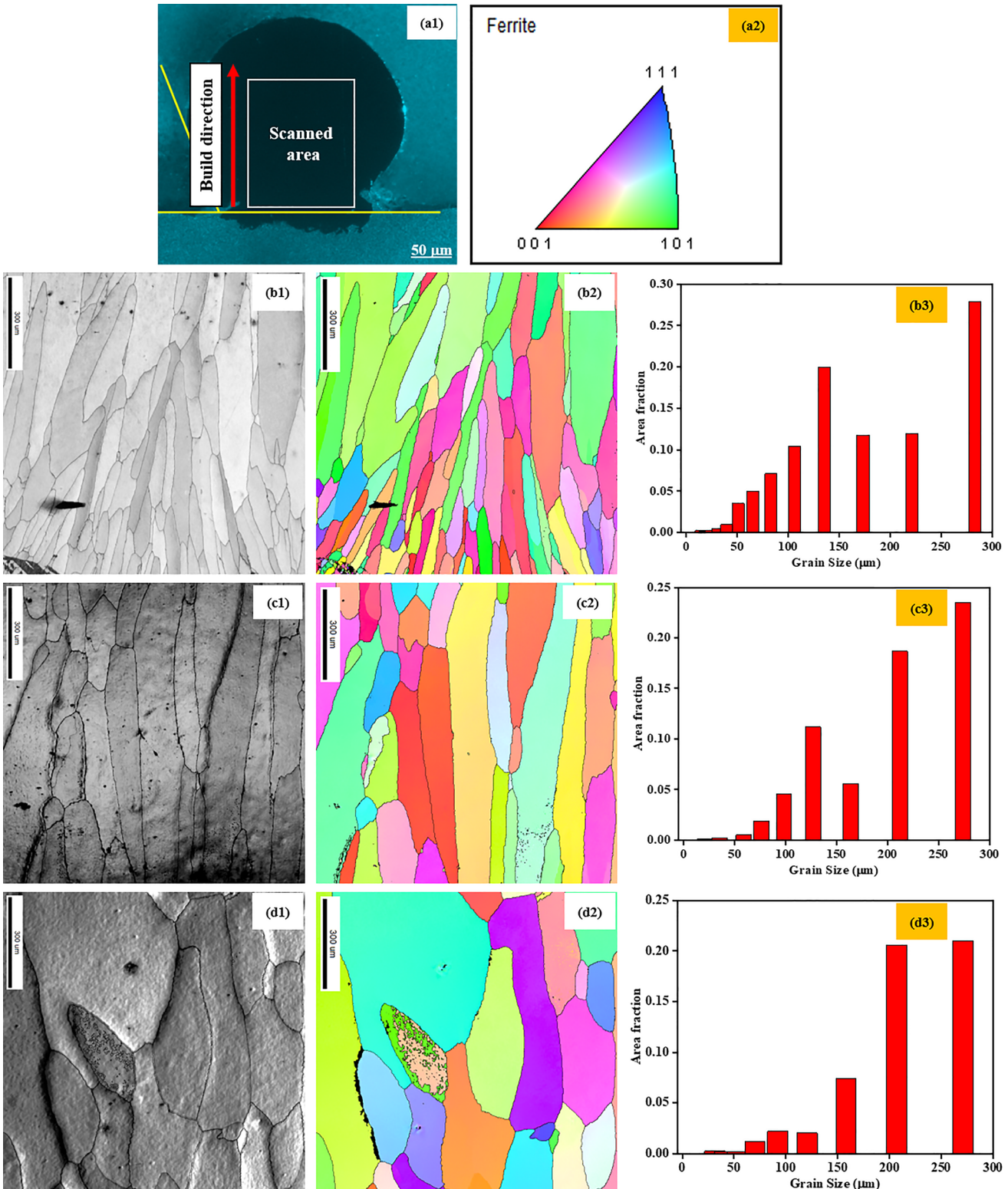


**Fig. 4** EBSD analysis of cross section for different cladding layer thicknesses: (a1) sectioned evaluation surface for analysis and (a2) orientation maps; band contrast maps, IPF and grain size distribution: (b1, b2 and b3) for 1 mm thick layer, (c1, c2 and c3) for 2 mm thick layer and (d1, d2 and d3) for 3 mm thick layer, respectively

was no obvious preferred orientation and the grain orientations were randomly distributed.

The BC and IPF maps depict that the grains in the cross section of cladding layers were mostly coarse and grew along

the structural direction. The similar observation was also reported by a few researchers (Ref 25). Peng et al. (Ref 25), observed that the temperature gradient component perpendicular to the boundary of the molten pool was high compared to

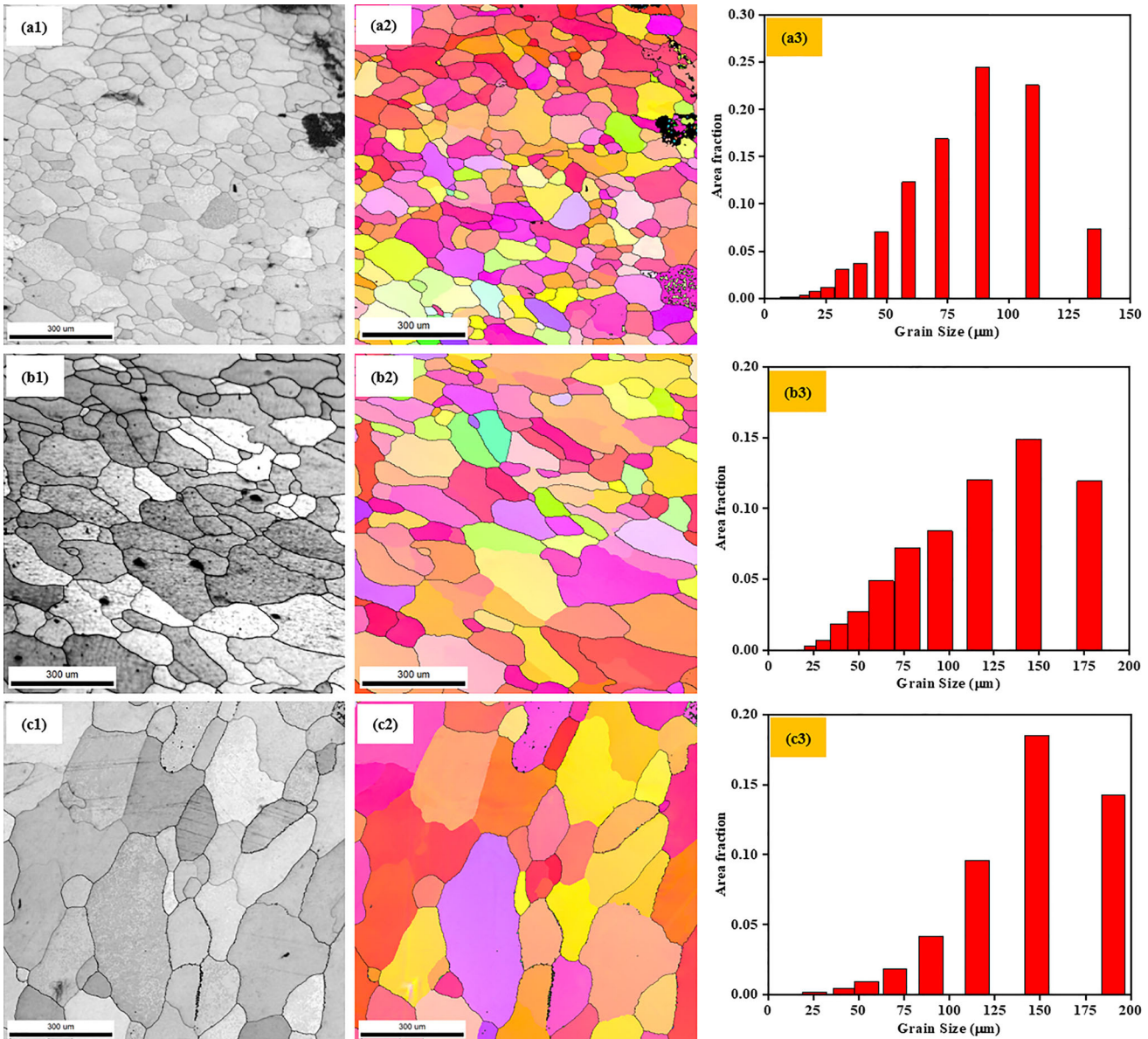


**Fig. 5** EBSD analysis of top surface for different cladding layer thicknesses: band contrast maps, IPF and grain size distribution: (a1, a2 and a3) 1 mm (b1, b2 and b3) 2 mm (c1, c2 and c3) 3 mm, respectively

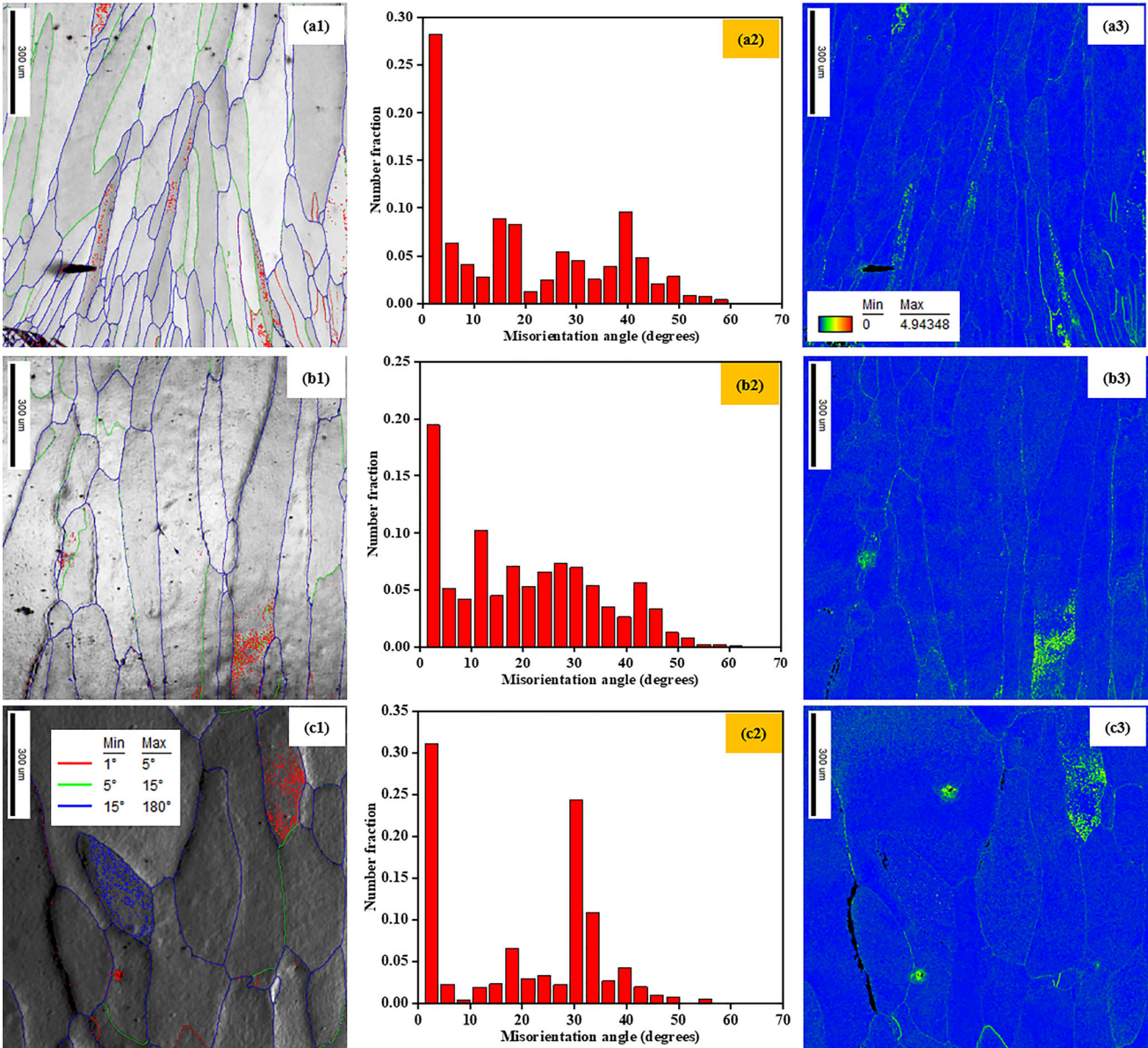
other directions. This temperature gradient discrepancy resulted in directional grain growth. Additionally, Fig. 4(b2, c2, and d2) illustrate the presence of columnar grains in the cladding layers, which exhibited growth along a direction perpendicular to the fusion line. This direction of grain growth coincided with the direction of the temperature gradient.

Figure 4(b3, c3 and d3) show the grain size in cladding layers in the cross sectional area. The grain size distribution of the full section was computed using EBSD post-processing software to determine the grain size. The average equivalent circle diameter of each grain served as the measure of grain size. From grain size analysis, the average minimum grain size of 65  $\mu\text{m}$  was observed in the 1 mm cladding layer, compared to 78  $\mu\text{m}$  and 98  $\mu\text{m}$  in the 2 and 3 mm cladding layers, respectively.

The EBSD analysis of the top surface of the cladding layers are shown in Fig. 5. The BC and IPF maps of the grains of the top surface are shown in Fig. 5(a1, b1 and c1) and Fig. 5(a2, b2

and c2), respectively. The color patterns of grains in different sizes are depicted in all the samples in the IPF maps in Fig. 5(a2, b2 and c2). Different cooling rates and solidification temperatures caused variations in the grain size and orientation in all of the cladding layers of the deposited specimens. Fig. 5(a3, b3 and c3) show the grain size of the top surface of cladding layer. The average smallest grain size of 40  $\mu\text{m}$  was observed in 1 mm cladding layer, with more than 75 % of them below 50  $\mu\text{m}$  grain size. In the 2 mm thick layer, 60% and in 3 mm layer 50% grains are less than 50  $\mu\text{m}$  grain size. The average grain size of 2 and 3 mm cladding layer was of 69 and 87  $\mu\text{m}$ , respectively.

Grain size of cladding metals is significantly influenced by cooling rate. In general, it is accepted that greater undercooling at higher cooling rates results in smaller grains. Higher cooling rates reduces the ferrite grain size and also aids high strength, hardness, dislocation density, and fine phases as it suppresses the atomic diffusion. On the other hand, slow cooling rates lead



**Fig. 6** EBSD analysis of cross section of different cladding layer thickness: grain boundary maps, misorientation angle distribution and KAM maps; (a1, a2 and a3) 1 mm, (b1, b2 and b3) 2 mm, (c1, c2 and c3) 3 mm, respectively

to transformation into soft, coarse, and less dislocated phases like polygonal ferrite, which is mostly observed in 3 mm cladding layer. The development of different phases due to difference in cooling rates are briefly discussed in Section 3.3.2 and Section 3.3.3.

The low-angle grain boundaries (LAGBs) and high-angle grain boundaries (HAGBs) in both cross section and top surface of cladding layers are shown in Fig. 6(a1, b1 and c1) and Fig. 7(a1, b1 and c1), respectively. LAGBs are represented on color maps in red and green; while, HAGBs are represented on color maps in blue. A misorientation angle  $\geq 15^\circ$  was used to distinguish HAGBs from LAGBs. In the cross section of cladding layers, the proportion of LAGBs observed is 51% in 1 mm cladding layer (Fig. 6a2). The LAGBs % are of 44 and 38 on 2 mm (Fig. 6b2) and 3 mm (Fig. 6c2) cladding layer, respectively. In top surface of cladding layers, the proportion of LAGBs observed is 41% in 1 mm cladding layer (Fig. 7a2).

The LAGBs % are 39 and 34 for 2 mm (Fig. 7(b2)) and 3 mm (Fig. 7(c2)) cladding layer, respectively. At the macro level, the presence of LAGBs contributed to the strengthening of the material. The abundance of LAGBs impeded the motion of dislocations during the stretching process, leading to an increase in the overall strength of the sample. This strengthening effect is expected to be evident in subsequent mechanical performance tests.

The kernel average misorientation (KAM) of cross section and top surface of the deposited cladding layers derived from the EBSD data are shown in Fig. 6(a3, b3 and c3) and Fig. 7(a3, b3 and c3), respectively. The KAM diagrams depict the strain by calculating local grain misorientations. The green regions in Fig. 6(a3, b3 and c3) and Fig. 7(a3, b3 and c3) represents significant strain development, which are mainly distributed in the grain boundaries and sub-regions in the cladding layers. The average KAM values of all the cases were

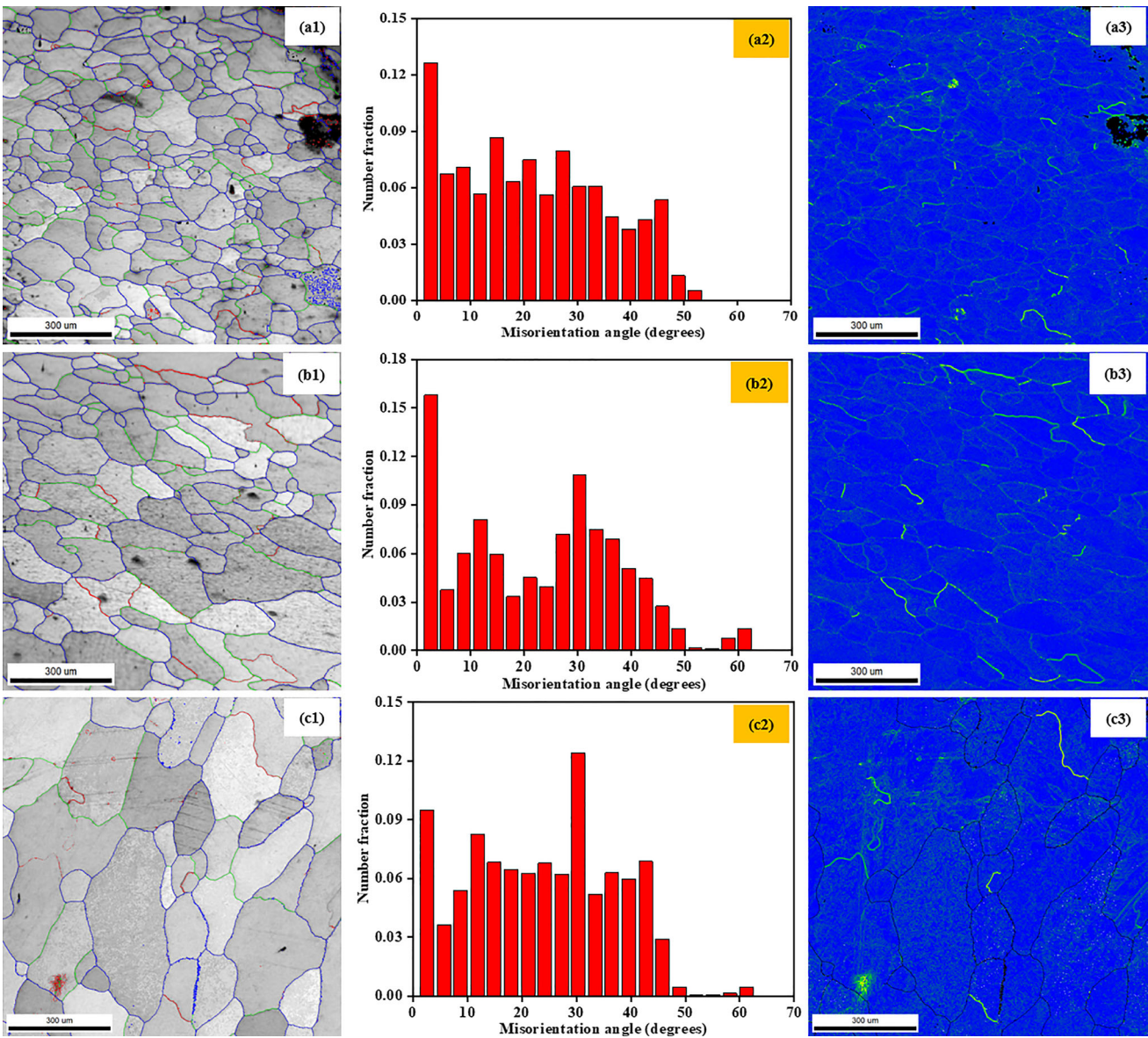


**Fig. 7** EBSD analysis of top surface for different cladding layer thickness: grain boundary maps, misorientation angle distribution and KAM maps; (a1, a2 and a3) 1 mm, (b1, b2 and b3) 2 mm, (c1, c2 and c3) 3 mm, respectively

concentrated in  $<2^\circ$ , with highest value reaching  $4.9^\circ$ . The average KAM value of a typically recrystallized structure is known to be  $<1^\circ$  (Ref 26), suggesting the presence of minimal residual strains within the structure. According to the current work, geometrically necessary dislocations (GNDs) have a positive correlation with KAM value, and their density may be calculated using the following formula (Ref 27):

$$\rho^{\text{GND}} = (\pi\theta)/(90\mu b), \quad (\text{Eq } 3)$$

where  $\theta$  is the average local misorientation angle in degree,  $b = 2.49 \text{ nm}$  is the Burgers vector,  $\mu = 1 \text{ }\mu\text{m}$  is the unit length (step size). The maximum dislocation density was of  $1.65 \times 10^{13} \text{ m}^{-2}$  was observed in the top surface of 1 mm cladding layer (with  $\theta = 1.18^\circ$ ). The dislocation density of  $1.59 \times 10^{13} \text{ m}^{-2}$  ( $\theta = 1.14^\circ$ ) and  $1.55 \times 10^{13} \text{ m}^{-2}$  ( $\theta = 1.11^\circ$ ) was observed in the top surface of 2 mm and 3 mm cladding layer, respectively. The dislocation density was

of  $1.52 \times 10^{13} \text{ m}^{-2}$  ( $\theta = 1.09^\circ$ ),  $1.50 \times 10^{13} \text{ m}^{-2}$  ( $\theta = 1.07^\circ$ ) and  $1.40 \times 10^{13} \text{ m}^{-2}$  ( $\theta = 1.01^\circ$ ) was observed in the cross section of 1 mm, 2 mm and 3 mm, respectively. Fig. 6(a3, b3 and c3) and Fig. 7(a3, b3 and c3) exhibits an inherent heterogeneity in the local misorientations throughout the structure, reflecting an uneven strains distribution. The cladding process involves rapid heating and cooling, causing localized expansion and contraction. This leads to the extrusion and collision of grains during the growth process, creating non-uniform stress and strain within the material. Thus, GNDs are generated as a mechanism to accommodate these differences and maintain continuity within the material (Ref 28). This helps to enhance the overall mechanical characteristics and structural integrity of the material, making it more resistant to failure.

**3.3.2 FESEM Observation.** The schematic showing X-Y-Z-axes of the cladding layers are shown in Fig. 8(a). The FESEM morphology of the top surface and cross section of

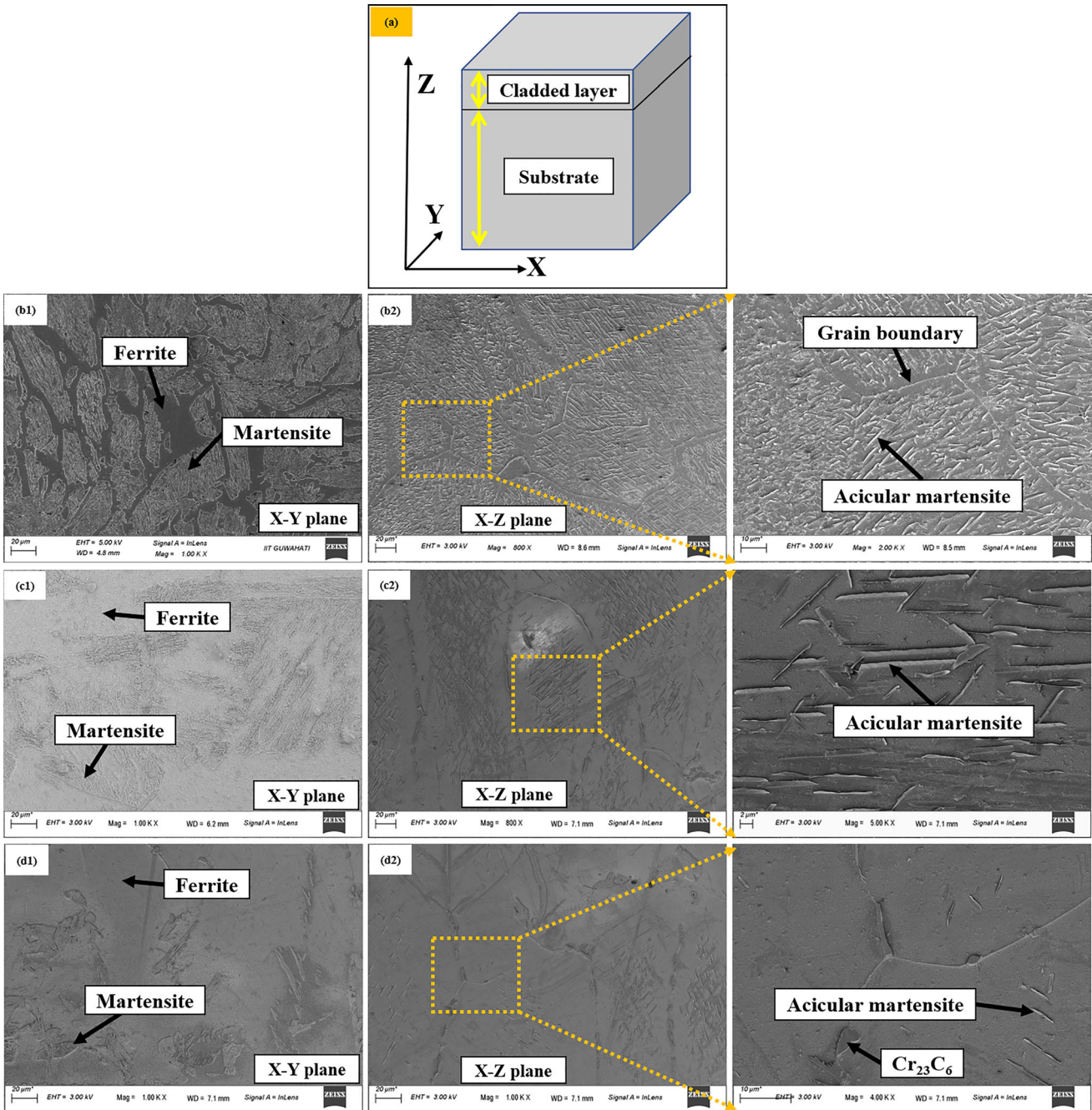


**Fig. 8** FESEM microstructure of top surface (*X-Y* plane) and cross section (*X-Z* plane) of different cladding layer: (a) schematic of *X-Y-Z*-axes, (b1, b2) 1 mm, (c1, c2) 2 mm and (d1, d2) 3 mm

different cladding layers are shown in Fig. 8(b1, c1 and d1) and (b2, c2 and d2), respectively. The observed morphology reveals the presence of distinct phases including ferrite, martensite, and acicular martensite. These different phases result due to rapid heating and cooling process employed in CMT cladding. The cooling of the cladding layers resembles a quenching process, leading to the formation of martensite at various locations within the structure. The extent of martensitic transformation during the cladding process was quantified using the image area method. The martensite phase at the top surface of 1 mm cladded layer was  $\sim 65\%$ ; it was  $\sim 49\%$  and  $\sim 31\%$  in 2 mm and 3 mm cladding layers, respectively. From the cross

sectional morphologies (Fig. 8 b2, c2 and d2), the presence of acicular martensite phase is also densely distributed in the 1 mm cladding layer compared to all others. The proportion of higher % of martensite transformation in 1 mm cladding layer owns to rapid cooling and high surface area to volume ratio compared to 2 mm and 3 mm cladding layer. The microstructure also depicts the presence of intergranular chromium carbides precipitates in the cross sectional morphology.

The EDS analysis of different cladding layers are shown in Fig. 9. The analysis depicts uneven distribution of present elements in the deposited cladding layers. The elemental mapping depicts clear segregation of elements corresponding to various phases in the micrographs. Fig. 9(b) illustrates the

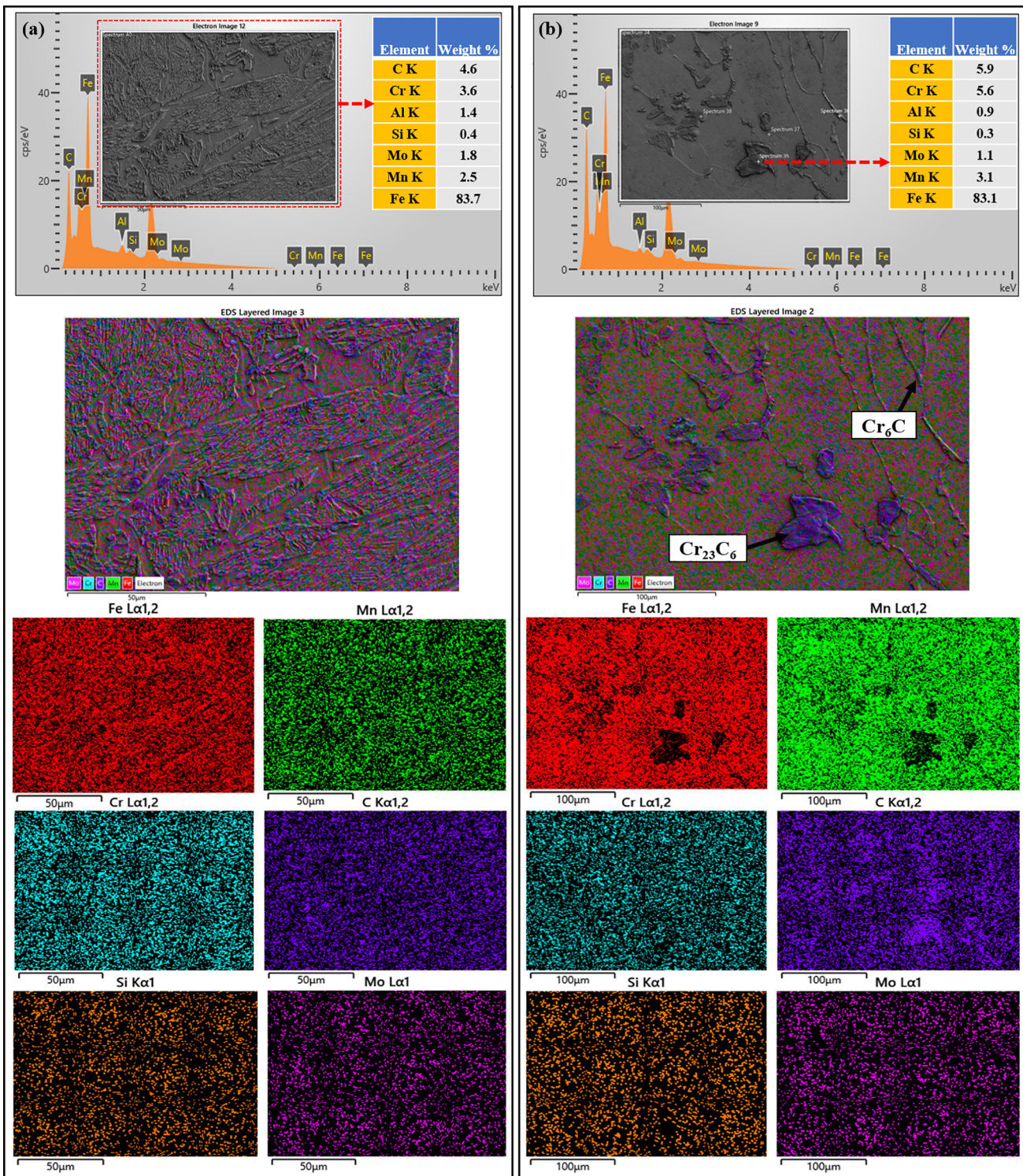


**Fig. 9** EDS analysis of different region: (a) top surface for 1 mm thick layer and (b) cross section for 3 mm thick layer

presence of secondary  $\text{Cr}_{23}\text{C}_6$  and  $\text{Cr}_6\text{C}$  carbide networks in certain regions. The wt.% concentration of Cr was also observed to be higher from the point EDS elemental distribution. In the elemental mapping, elevated levels of C and Cr in the concentrated Fe regions provide a clear indication of the existence of  $\text{Cr}_{23}\text{C}_6$  and  $\text{Cr}_6\text{C}$  carbides particles. This finding aligns with the observations reported by Mohammadnezhad et al. (Ref 29). The composition of deposited layer need not be

same as the filler wire due to phenomenon of dilution and segregation. Kumar et al. (Ref 30) similarly reported differences in elemental analysis during EDS analysis in the deposition of SS321/Inconel 625, noting composition 16.48% Mo, 40.35% Nb, and 10.40% Cr in the deposited layer compared to 8.4% Mo, 3.70% Nb, and 22.26% Cr in the filler wire. The welding process, particularly techniques like CMT, may change material composition after melting, solidification

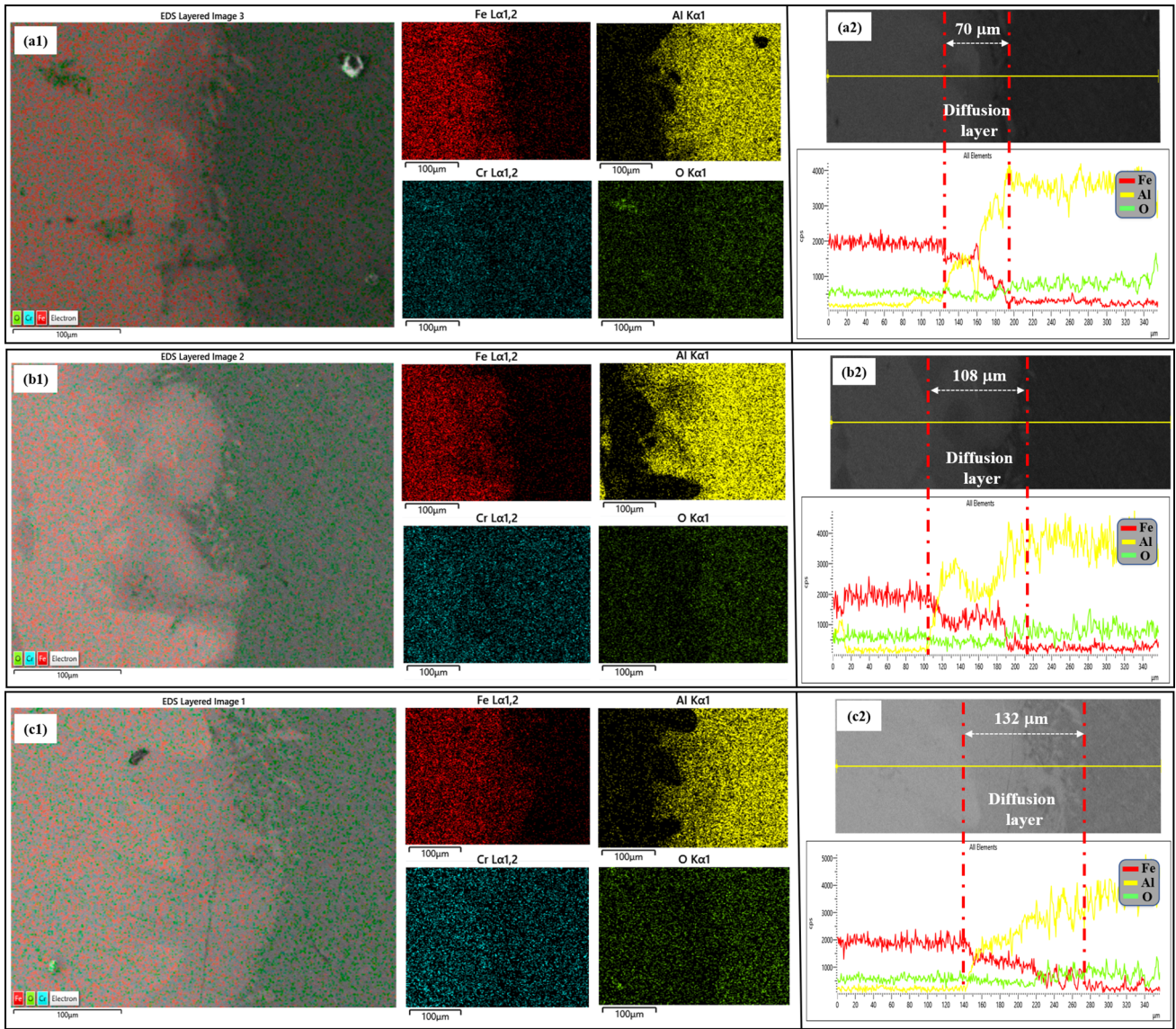


**Fig. 10** EDS analysis at the cross sections of cladding layers: (a) 1 mm (b) 2 mm and (c) 3 mm

and segregation. There is a possibility for secondary carbide phase formation during welding, especially evident in observed martensite structures. Again, the EDS analysis scrutinized elemental distribution at various locations within the deposited material; localized variations were revealed.

### 3.3.3 Interface Study and Volumetric Dilution Rate.

The elemental distribution of cladded samples along the cross section plane near the interface region of different layers are shown in Fig. 10. The EDS elemental mapping results across the interface region are shown in Fig. 10(a1, b1 and c1). EDS elemental mapping, especially the distribution of the Fe and Al, for the cladding joint (Fig. 10 a1, b1 and c1) suggests that the diffusion was mostly directed into the aluminum. This is reasonable since the diffusion coefficient of Fe into Al is more than that of Al into Fe at higher temperature (Ref 31). As a result, the intermetallic compounds (IMCs) layer was formed mainly on the aluminum side. The distribution of Cr across the interface in the EDS elemental maps also supports that diffusion occurred during cladding process. As a result of diffusion, effective joining

occurred at the interface under the plastic deformation.

During cladding of dissimilar alloys, the primary melted zone is prone to liquation cracks but no such defect was observed in the cladding layer interfaces as depicted from the magnified SEM imaging of Fe/Al interfaces (Fig. 10 a2, b2 and c2). The smooth and continuous interface indicates that a solid-state joining process occurred during cladding. Moreover, EDS line scan across the Fe/Al interfaces of the cladding layers (Fig. 10a2, b2 and c2) confirmed the atomic diffusion, indicating the formation of Fe/Al IMCs (Ref 32). Metallurgical bonds were formed as a result of the atomic diffusion across the joint interface. Based on the elemental distribution of line scan across interface (marked by dashdotted lines in the figure), the thickness of the diffusion layers was determined. An average diffusion layer thickness of 70, 108  $\mu\text{m}$  and 132  $\mu\text{m}$  was observed at the 1, 2 mm and 3 mm cladding layers, respectively. The higher diffusion layer in the 3 mm cladding was due to combined effect of high heat input and compressive stress (Ref 32). Based on the Al-Fe phase diagram (Ref 33) and EDS analysis, the possible IMCs formed at the interface were FeAl,

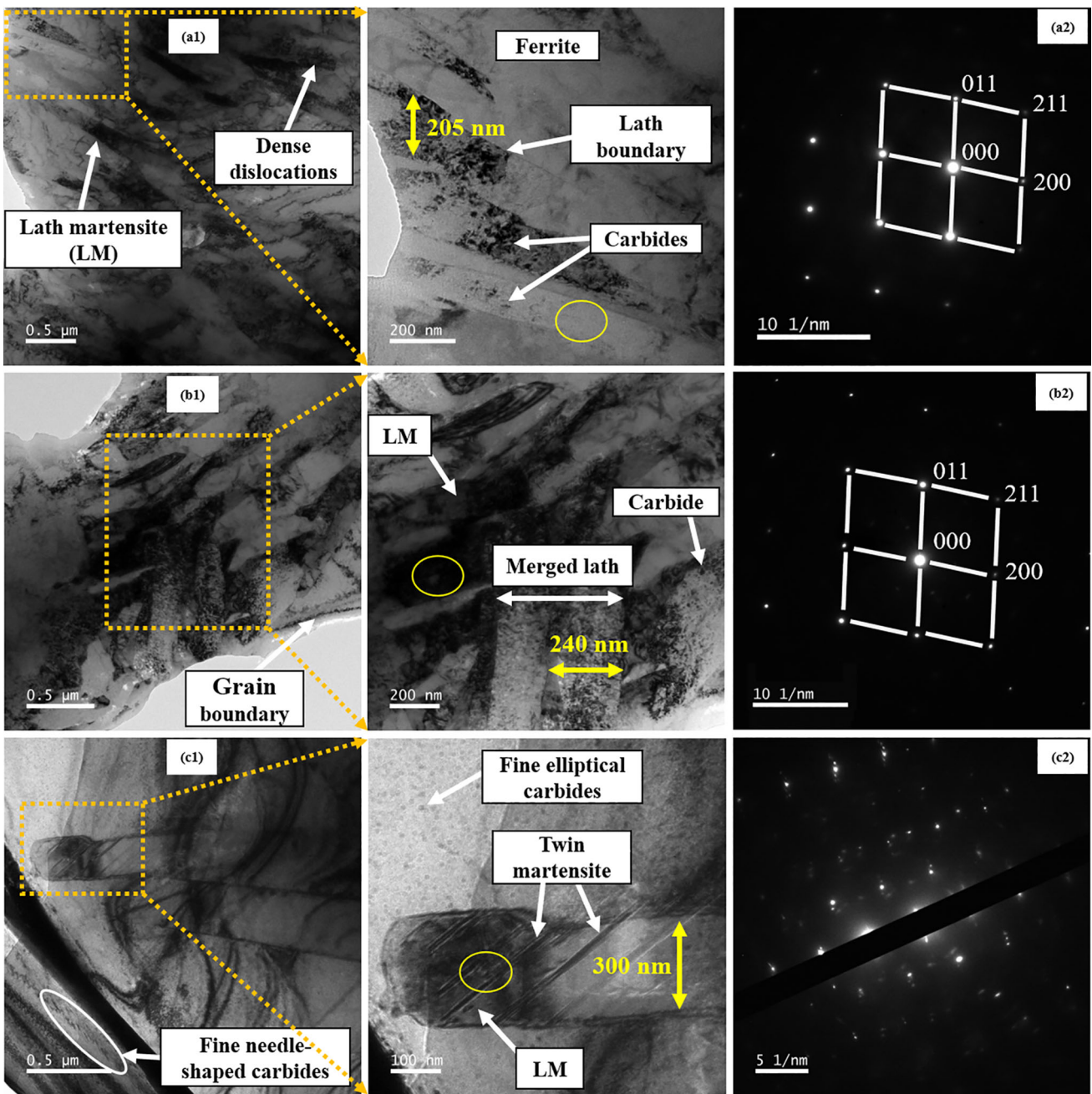


**Fig. 11** TEM microstructure of top surface and corresponding SAED patterns different cladding layers: (a1, and a2) 1 mm, (b1, and b2) 2 mm and (a1, and a2) 3 mm, respectively

$\text{FeAl}_3$ ,  $\text{Fe}_2\text{Al}_3$  and  $\text{Fe}_2\text{Al}_5$ . The similar IMCs were also reported by a few researchers (Ref 31-33).

**3.3.4 TEM Observation.** The TEM microstructural morphology at the top surface of cladding layers is shown in Fig. 11. The morphologies depict typical lath-type martensitic structure with dense dislocations and carbide precipitates. At a few locations merged lath martensite was also observed (Fig. 11 b1). The dislocation density is higher near the lath boundaries. The maximum average size of the lath martensite was found to be  $\sim 205$ ,  $\sim 240$  and  $\sim 300$  nm in 1, 2 and

3 mm cladding layers, respectively. The density of lath martensite was observed to be higher in 1 mm cladding layer. The aligned needle-like carbides appear at some specific angles within the martensite laths, as shown in Fig. 11(a1 and c1), which are believed to be  $\text{M}_2\text{C}$ -type carbides enriched with Mo and V formed during cladding process (Ref 34, 35). Fine elliptical carbides are also finely distributed in the structure (enlarged Fig. 11 c1), similar observation is also reported by Ju et al. (Ref 34). The selected area electron diffraction (SAED) pattern of the lath martensite is shown in Fig. 11(a2, b2).

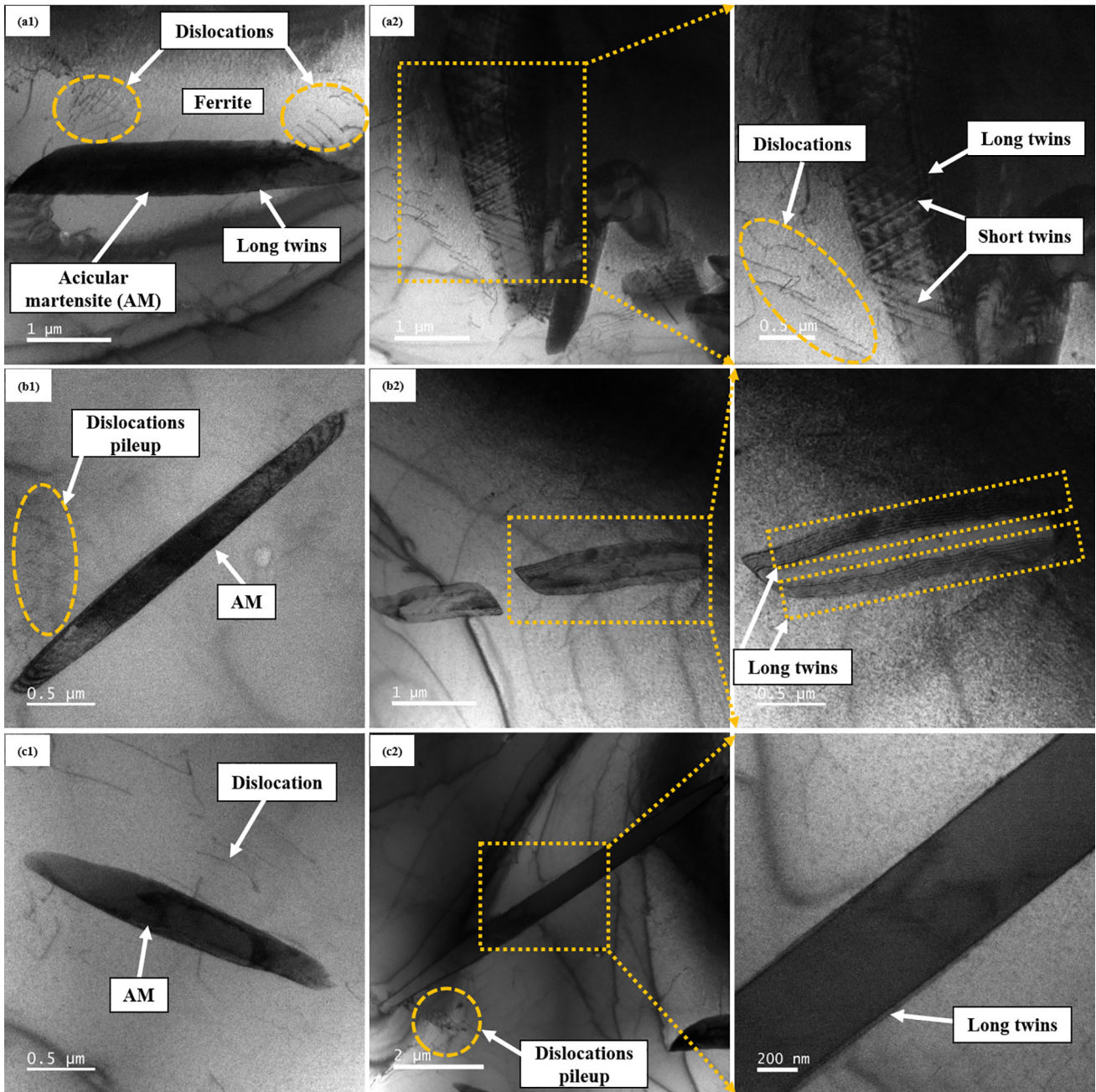


**Fig. 12** TEM cross sectional microstructure of different cladding layers: (a1, and a2) 1 mm, (b1, and b2) 2 mm and (a1, and a2) 3 mm, respectively

Distinct twin martensite is identified within the lath martensite as shown in the enlarged Fig. 11(c1) and the corresponding SAED pattern is shown in Fig. 11(c2).

The TEM morphology of cross section of different cladding layers are shown in Fig. 12. The TEM bright field morphology depicts distribution of ferrite and acicular martensite (AM) in accordance with the FESEM morphology of cross section (Fig. 8). The AMs densely surrounded by fine dislocation lines are clearly revealed in all the bright field images. Dislocation lines are more pronounced in 1 mm thick layer than in 2 mm and 3 mm layers. Each AM plate in the microstructure is

composed of a high density of twinning substructure. Long and short twinned martensite structure is identified in (enlarged Fig. 12 a2, b2 and c2) some locations in AM; these must have been formed during the final cooling, as the martensitic transformation in carbon steels often accompanies formation of twins to accommodate the transformation strains (Ref 36).

### 3.4 Phase Study

The phases and compounds developed in the different cladding layers has been analyzed using XRD and XPS, respectively. The phases developed in the top surface of

cladding layers are shown in Fig. 13. The XRD patterns reveals the presence of body-centered cubic (BCC, ferrite) lattice of  $\alpha$ -Fe phase corresponding to  $2\theta$  value of  $44.43^\circ$ ,  $64.77^\circ$ ,  $81.90^\circ$  as per JCPDS-96-901-3477. The similar phases are observed in all

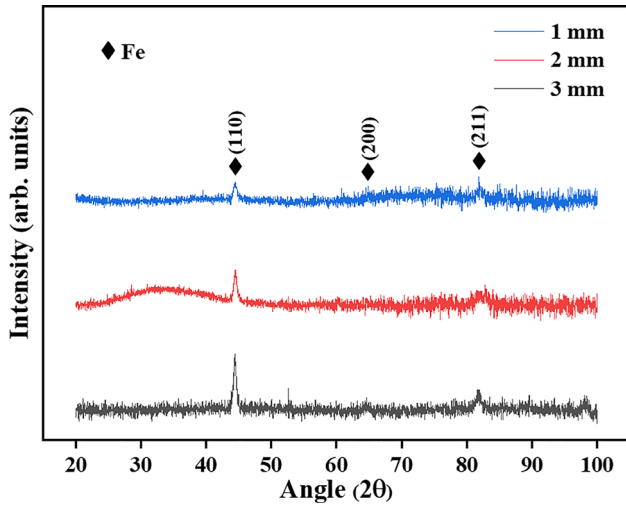


**Fig. 13** XRD plots at the top surface of different cladding layers

the cladding layer. Since XRD could not detect the presence of compounds, further detection was carried out through XPS.

Figure 14 shows the XPS plots of different cladding layers. The plots depict the spectra of fabricated elements, bonding states and chemical structure. The survey spectrum in XPS plots show the presence of Fe 2p, Cr 2p, O 1s, C 1s, and Fe 3p in the cladding layers. The XPS spectra of the three different cladding layers depict that the signal peak trend in the cladding layer is consistent. The high-resolution spectra of present elements (Fe 2p, Cr 2p, O 1s and C 1 s) are shown in Fig. 15(a-d), which are obtained through curve fitting. The peak splitting depicts, the binding energy values of 706, 711 and 717 eV corresponding to Fe 2p (Fig. 15a), which represents the existence of metallic Fe at 706 eV and  $\text{Fe}_2\text{O}_3$  at 711 and 717 eV in the cladding layer. Figure 15(b) depicts the splitting of Cr 2p into  $\text{Cr}_2\text{O}_3$  at the binding energy values of 578 and 587 eV. Figure 15(c) shows the O 1s energy spectrum constitutes binding energy peaks of 527, 531 and 537 eV, which corresponding to O at 531 eV and  $\text{O}_2$  at 527 and 537 eV. Finally, C-C, C-O, and O-C=O bond in the C1s peak (Fig. 15d), corresponding to binding energy values at 283, 285 and 288 eV, respectively. Similar outcomes with insignificant variations in the binding energy values are also seen in the 2 mm and 3 mm cladding layers, as also reported by a few researchers (Ref 37, 38). According to the literature (Ref 39), the presence of  $\text{Fe}_2\text{O}_3$  and  $\text{Cr}_2\text{O}_3$  compounds in the steel acts as

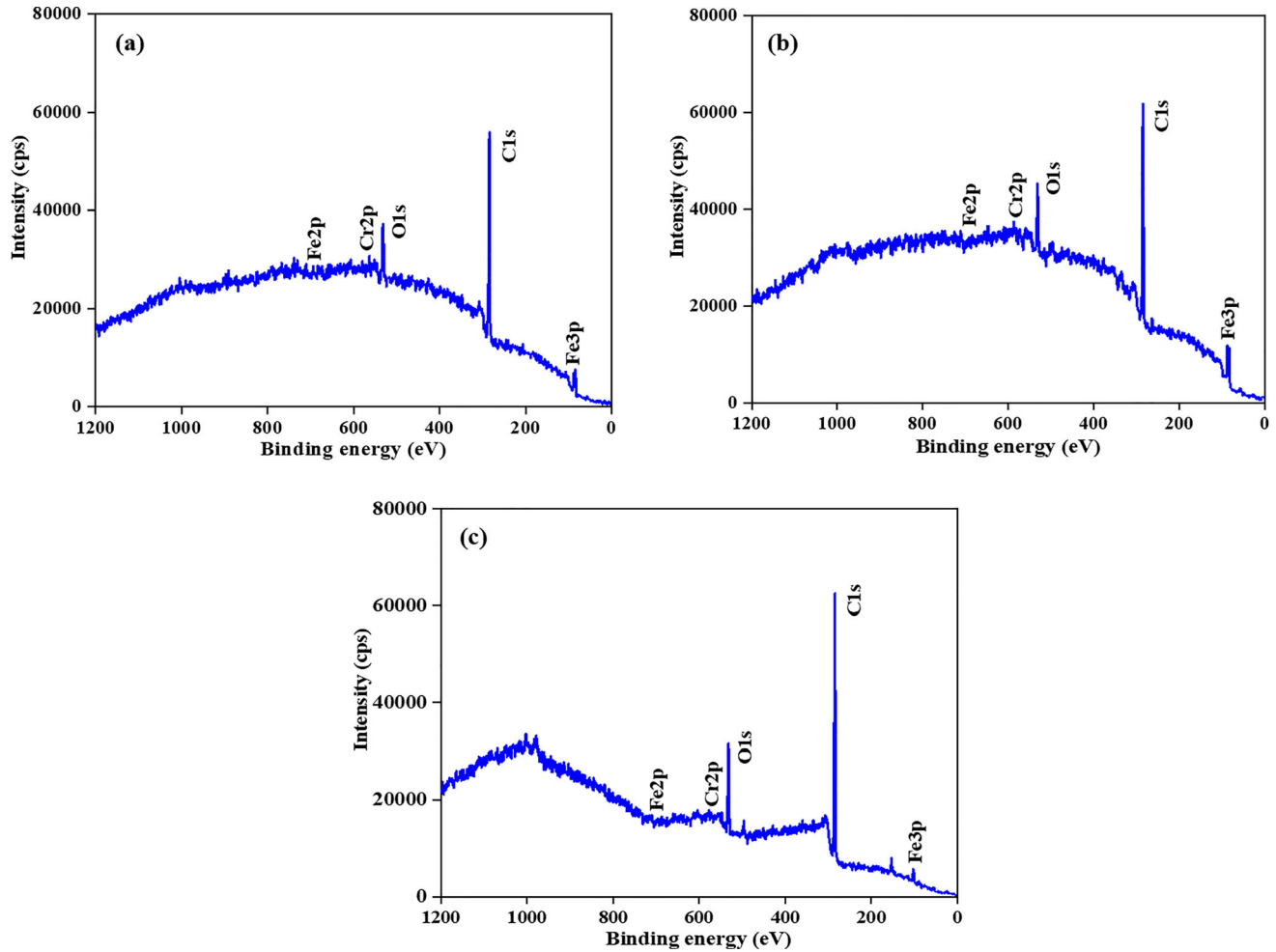


**Fig. 14** XPS spectra of cross section of different cladding layers: (a) 1 mm, (b) 2 mm and (c) 3 mm

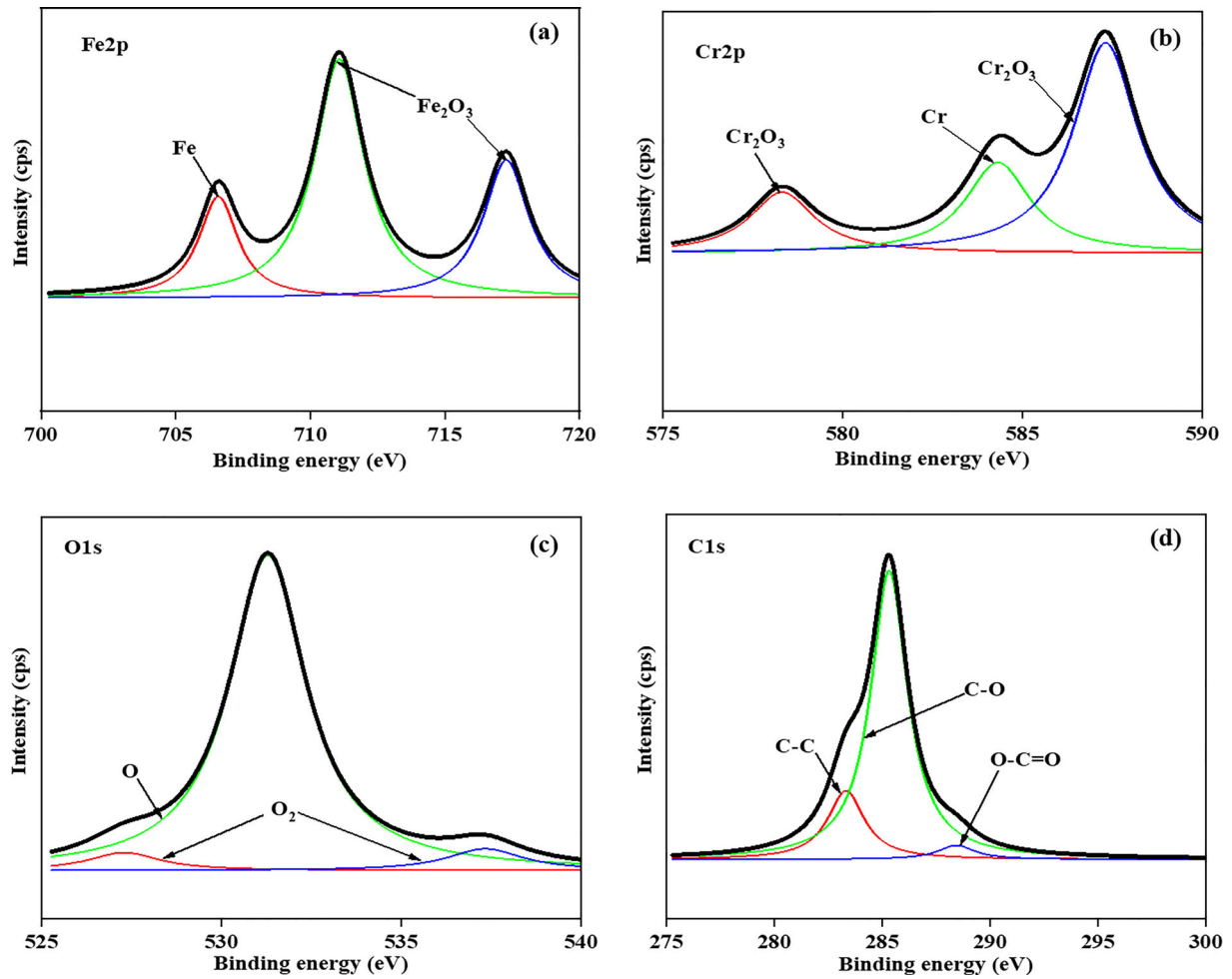


**Fig. 15** High resolution XPS spectra of different elements: (a) Fe 2p, (b) Cr 2p, (c) O 1s and (d) C 1s

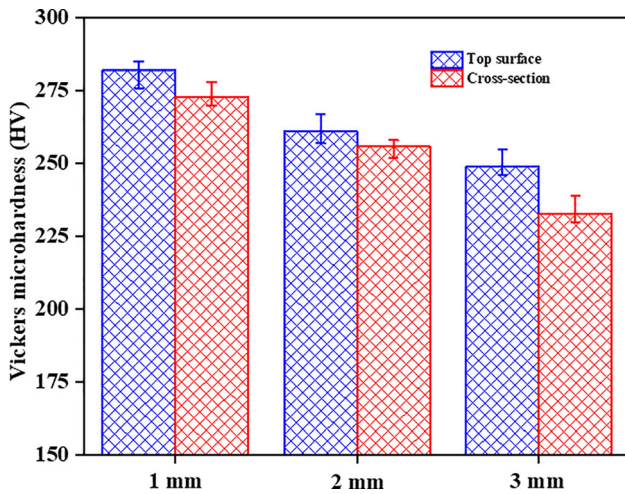


**Fig. 16** Microhardness of deposited cladding layer of different thickness

a protective film and aids in enhancement of different mechanical properties.

### 3.5 Hardness Study

Figure 16 shows the Vickers microhardness values of the different cladding layers. The variation of hardness in the cladding layers are because of strengthening mechanisms; grain boundary strengthening, dislocation strengthening, transformation strengthening and solid solution hardening. EBSD grain size analysis in Fig. 4(c1, c2 and c3) and 5(c1, c2 and c3) reveals that cladding thickness affects grain size. The 1 mm cladding thick cladding layer resulted in finer grains, thus increasing the microhardness. The greatest value of microhardness is 282 and 273 HV for 1 mm cladding layer on top surface and cross section with 40  $\mu\text{m}$  and 65  $\mu\text{m}$  grain sizes, respectively. The lowest value of microhardness was 249 and 233 HV for 3 mm cladding layer on top surface and cross section with 87  $\mu\text{m}$  and 98  $\mu\text{m}$  grain sizes, respectively. The presence of numerous grain boundaries in the fine-grained structure impedes the movement of dislocations, resulting in an increase in microhardness (Ref 40). The grain boundary strengthening mechanism is effectively described by the Hall–Petch relation (Ref 41, 42).

$$H = H_0 + \frac{k_H}{\sqrt{d}}, \quad (\text{Eq 4})$$

**Table 2** Wear values of different thickness cladding layer

Sample	Wear mass loss, gm	Mean wear depth, $\mu\text{m}$	Wear volume, $\text{mm}^3 \times 10^{-3}$	Hardness, HV	Coefficient of friction	Lancaster wear coefficient, $\text{mm}^3/\text{Nm} \times 10^{-5}$
1 mm	+0.9 3.2 –0.8	+4 31 –2	+0.05 0.41 –0.03	+3 282 –6	+0.06 0.19 –0.05	+0.08 0.88 –0.05
	+1 3.6 –0.7	+4 35 –2	+0.05 0.46 –0.03	+6 261 –4	+0.03 0.21 –0.02	+0.09 0.99 –0.04
	+0.6 3.8 –1.5	+3 41 –4	+0.04 0.48 –0.03	+6 249 –3	+0.04 0.24 –0.02	+0.08 1.03 –0.03
2 mm						

where  $H_0$  and  $k_H$  are material constants,  $H$  is the hardness,  $d$  is the average grain diameter. To evaluate the validity of relation, the  $H_0$  and  $k_H$  are derived using the hardness and average grain size of two cladding layers: one with a 1 mm thickness and the other with a 3 mm thickness. These cladding layers represent the two extremes in terms of hardness. Although data-fitting techniques perform well in interpolation, they tend to yield significant errors when extrapolating. Therefore, the values of  $d$  and  $H$  were substituted into Eq 4 to form two simultaneous linear equations based on the average measurements from the 1 mm and 3 mm cladding layers. Accordingly, for the top surface  $H_0 = 179 \text{ MPa}$ ,  $k_H = 648 \text{ MPa}\sqrt{\mu\text{m}}$  and for the cross section:  $H_0 = 57 \text{ MPa}$ ,  $k_H = 1738 \text{ MPa}\sqrt{\mu\text{m}}$ . Using these values, the interpolated hardness values for 2 mm thick layer are determined to be 257 and 254 HV for the top surface and cross section, respectively. The corresponding measured microhardness values are 261 and 256 HV, indicating a good agreement. This demonstrates that the Hall–Petch relation offers a reliable estimation of hardness.

According to EBSD analysis, the difference in hardness is also caused by dislocation strengthening. The enhanced hardness in 1 mm thick cladding were also related to higher number of LAGBs (Fig. 6 and 7) compared to 2 and 3 mm cladding layer. From KAM maps, the higher number of dislocations were observed in LAGBs. Thereafter, the cladding layer with 1 mm thickness in both top and cross section has higher dislocation density owing to higher number of LAGBs.

According to FESEM (Fig. 8) and TEM morphology (Fig. 11 and 12), the variation in microhardness values can be attributed to transformation strengthening. The enhanced microhardness in 1 mm cladding layer attributes to higher martensitic structure as compared to 2 and 3 mm cladding layer. The twins in the martensite structure are pronounced in 1 and 2 mm cladding layers (Fig. 12). Das et al. (Ref 43) also stated that increase in the dislocations and twin boundaries in the sample enhances the hardness. However, due to presence of ferritic structure and low proportion of martensitic transformation in the 2 and 3 mm cladding layer, the hardness is low. Further, the cooling rate of 1 mm cladding was higher than that of 2 and 3 mm cladding layers. The relationship between microhardness and cooling rate as well as carbon content is well-known, where an increase in both parameters leads to solid solution hardening and subsequently higher microhardness (Ref 44).

### 3.6 Wear Study

The wear mass loss of different cladding layer thickness is represented in Table 2. The reduced mass loss experienced by

the 1 mm cladding layer can be attributed to its high hardness. On the other hand, the 2 and 3 mm cladding layers exhibit higher mass loss due to the surface's softness, which results in substantial plastic deformation during sliding against the steel surface. In contrast, the surface of the 1 mm cladding layer comprises a uniform and finely dispersed distribution of hard martensite. The presence of hard debris generated during sliding serves as asperities on the worn surface, reducing the actual contact between the surfaces of the cladding layer and the hardened steel. These debris and the reduced grain boundaries create a significant obstacle in the removal of material during dry sliding. Furthermore, due to the heat generated by the sliding motion between the pin and disc, an oxide layer is formed, which prevents direct metal-to-metal contact by acting as a barrier.

The mean wear depth, wear volume, coefficient of friction (CoF) and Lancaster wear coefficient values of different cladding layer thickness are represented in Table 2. The enhanced strengthening mechanisms and fine grain effects in 1 mm cladding layer are accountable for low wear depth and volume. The EBSD and TEM investigation showed higher dislocations in 1 mm thick cladding layer. As the dislocation density increases, the mobility of dislocations becomes restricted, resulting in an increase in hardness. Hardness and wear volume are inversely associated in both adhesive and abrasive wear modes, as evident in Table 2. The data presented in Table 2 confirms that materials with higher hardness demonstrate lower wear volumes. The wear equation proposed by Archard (Ref 45) is expressed as follows:

$$V = K \frac{F_n s}{H}, \quad (\text{Eq 5})$$

where  $V$  denotes the wear volume,  $s$  is sliding distance,  $F_n$  is applied load,  $H$  is hardness and  $K$  is a coefficient. For each case  $K$  is obtained approximately as  $2.5 \times 10^{-5}$  unit.

The elevated CoF observed in the 3 mm cladding layer can be attributed to its relatively low hardness. Additionally, the frictional heat generated during dry sliding wear between the cladding layer and hardened steel causes the contact surface to become softer. Consequently, debris forms at the contact surface, leading to increased CoF values as a result of ploughing and abrasion (Ref 46). In 1 mm cladding layer due to enhanced hard martensitic structure the development of debris is less and consequently low friction. Additionally, a harder surface experiences less friction resistance since it offers less adhesive contact area for a fixed load. The minimum Lancaster wear coefficient was observed in 1 mm cladding layer ( $0.88 \times 10^{-5} \text{ mm}^3/\text{Nm}$ ) compared to 2 and 3 mm

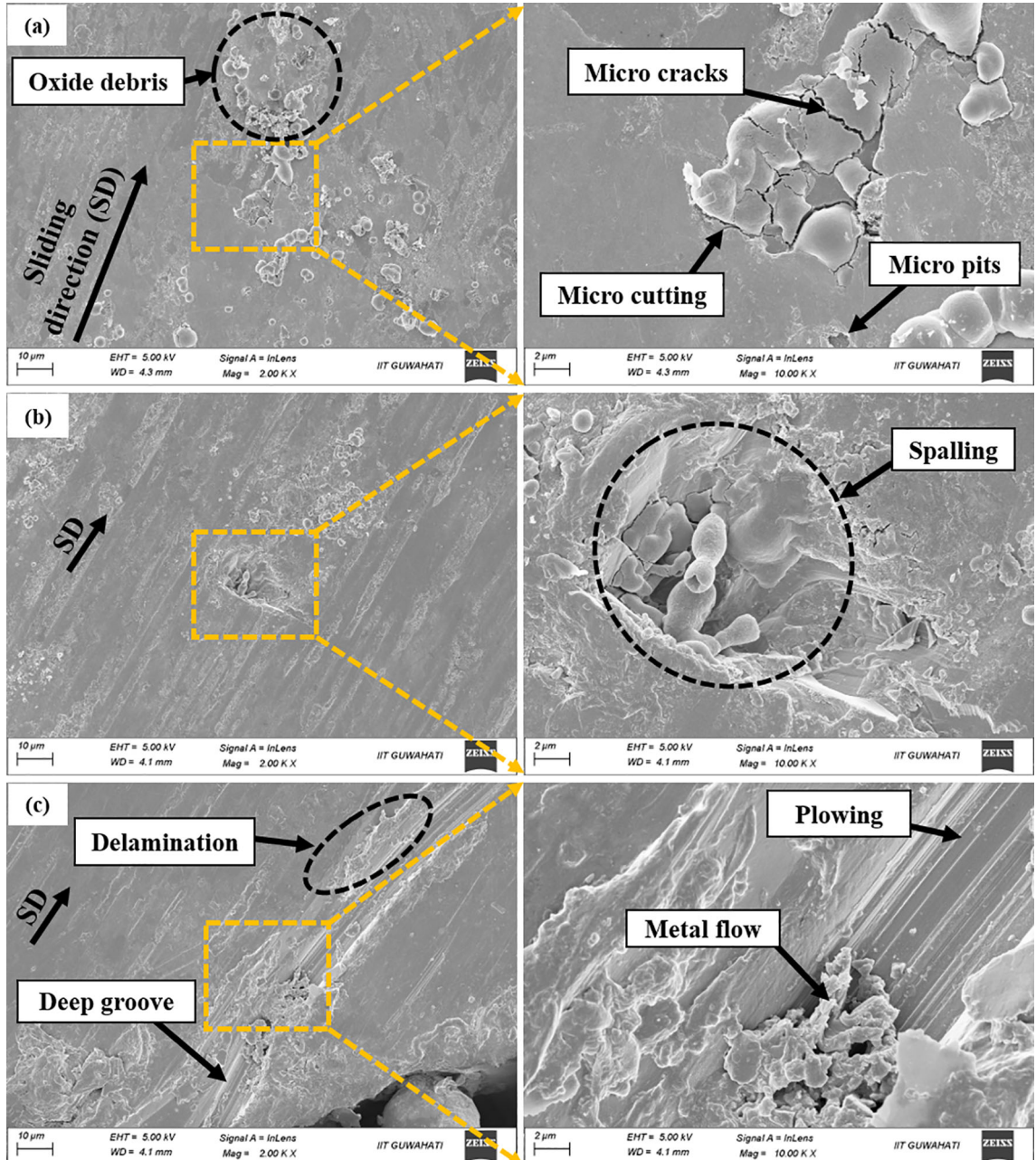


**Fig. 17** FESEM wear micrographs of deposited cladding layer of different thicknesses: (a) 1 mm, (b) 2 mm and (c) 3 mm

cladding layer. The Lancaster wear coefficient was calculated as (Ref 47):

$$k = \frac{V}{F_n s}. \quad (\text{Eq } 6)$$

The lower the value of  $k$ , the higher is the wear resistance. Table 2 shows that  $k$  is higher for softer material.

The FESEM morphologies of worn-out surfaces are shown in Fig. 17. The morphologies are different for different cladding layer thicknesses. Evidence of the existence of pores, scratches, and grooves were observed in all morphologies. However, 3 mm cladding layer displayed a substantial degree of surface wear compared to 1 and 2 mm cladding layer, which could potentially result in crack development. The extensive wear of 3 mm cladding layer can be attributed to its low hardness,

which causes an increase in wear volume, Lancaster wear coefficient, and abrasive wear compared to those in 1 and 2 mm thick cladding layers. Some areas of the wear track of the cladding exhibit localized peeling off of layers, micro pits and delamination phenomena, which inferred to abrasive and adhesive wear mechanism. During the wear process, localized porosities aggregate, which accelerates cracking followed by wear loss. The higher grain boundary area and LAGBs in 1 mm cladding layer may resist deformation during wear, which in turn reduces wear loss. The presence of oxide debris observed on the worn surface indicates a substantial level of oxidation occurring during the wear process. On the cladded worn surface, the Fe oxide was found to be easily scraped off and transferred as secondary abrasive particles, which intensified the abrasive wear during sliding. Additionally, the frictional

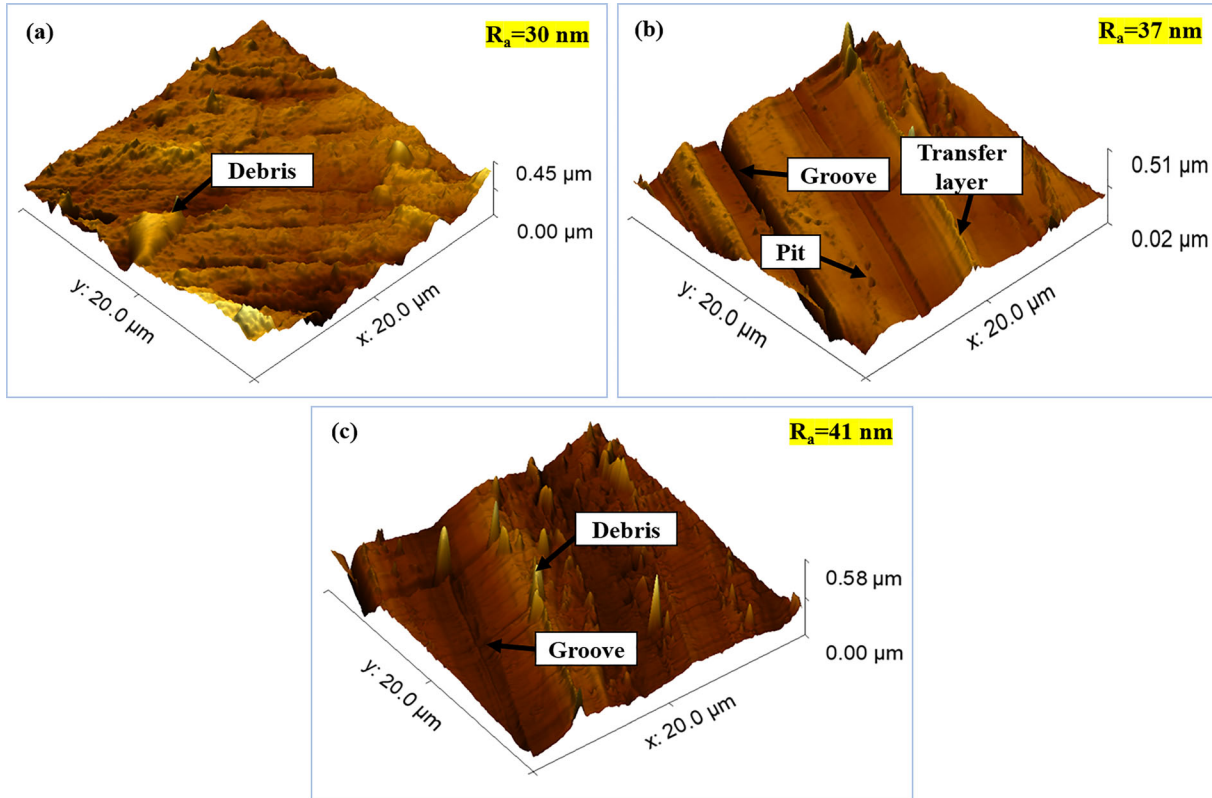


**Fig. 18** Surface roughness of deposited cladding layer of different thickness: (a) 1 mm, (b) 2 mm and (c) 3 mm

heat generated during dry sliding wear caused a rise in temperature, resulting in a relative softening of the contact surface between the cladding layer surface and its counterpart. This softening led to an increased accumulation of debris on the friction surface, which produced more visible micro-cuts. The accumulation of worn debris from adhesive wear further facilitated three-body abrasive wear (Ref 48). From the surface morphology of the wear track and Lancaster wear coefficient analysis, it is evident that enhanced hardness and LAGBs protects the surface from wear and improves the wear resistance in 1 mm cladding layer.

Figure 18 shows the 3D AFM morphology of the worn surface, depicting the presence of wear tracks, debris, grooves, and pits. The sudden rise in peak height can be attributed to wear debris; while, the valleys correspond to grooves, pits, and tracks. This morphology indicates a significant amount of plastic deformation occurring during wear. Among the different cladding layer surfaces, the 1 mm cladding layer exhibited the smallest increase in peak-to-valley distance compared to the 2 and 3 mm layers. The surface roughness was quantified using the average  $R_a$  value, which was found to be 30 nm for the 1 mm cladding layer, 37 nm for the 2 mm cladding layer, and 41 nm for the 3 mm cladding layer. The surface area affects the  $R_a$  value (Ref 49). The higher increase in  $R_a$  value is associated with the higher CoF. The 1 mm cladding layer, with its enhanced hardness and minimal plastic deformation, displayed a smoother surface and a lower  $R_a$  value. The surface roughness was measured within a scanned area of  $400 \mu\text{m}^2$ .

Figure 19 shows the morphologies of wear debris from different cladding layers. The micrograph exhibits a variety of shapes, including regular, irregular, spherical, elongated, and curled forms. The presence of regular-shaped debris in the 1 mm cladding layer suggests that material removal occurred through rubbing and mild adhesion. These smaller debris particles possess smooth surfaces and edges (Fig. 19 a1, a2). In contrast, the irregular-shaped debris in the 2 mm cladding layer indicates material removal through severe sliding and fatigue. These larger debris possess rough surfaces and irregular sharp-edge (Fig. 19 b1, b2). The elongated and curled shapes of the debris in the 3 mm cladding layer suggest material removal through cutting and plowing actions. Fig. 19(c1, c2) reveals that the sharp edges of the debris contributed to the cutting and plowing actions. The presence of irregular, elongated, and curled debris shapes in the cladding layers indicates lower hardness, as observed in the 2 and 3 mm layers. Furthermore, the spherical-shaped debris in the cladding layers signifies material removal through sliding and grinding. The investigation of debris morphologies can be used for condition monitoring (Ref 50). Fig. 19(d1, d2 and d3) shows the point EDS analysis of the wear debris of 1 mm cladding layer. The elements distribution at two different points detected higher peak of oxygen, which depicts oxidation during the wear mechanisms. The higher amount of iron oxide and chromium oxide also had developed as they share the same peak with oxygen. The XPS analysis also reported the development of iron oxide and chromium oxide in the cladding layers. These

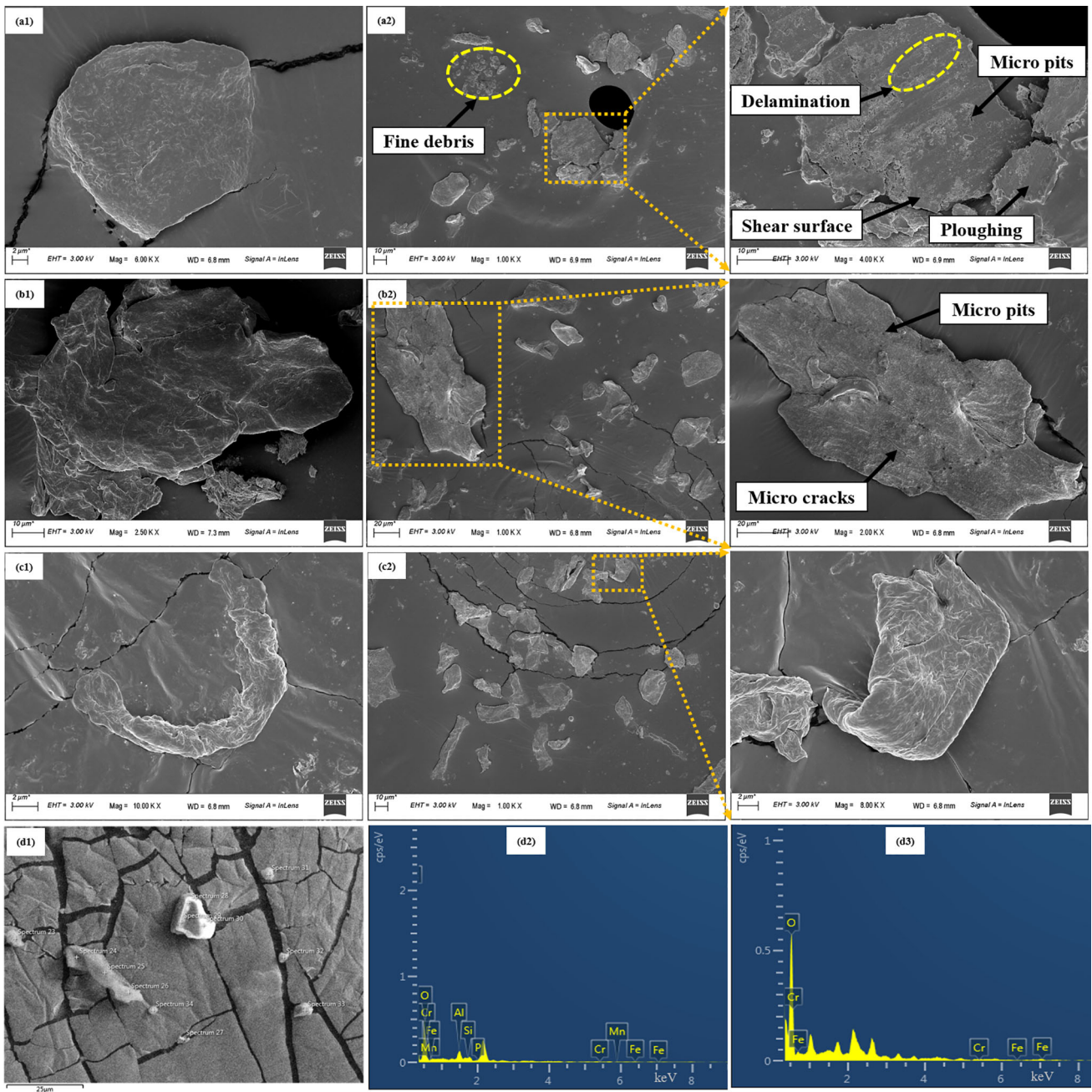


**Fig. 19** Morphology of wear debris of different cladding layers: (a1, a2) 1 mm, (b1, b2) 2 mm and (c1, c2) 3 mm; point EDS analysis of wear debris of 1 mm cladding layer: (d1) microstructure and (d2, d3) elemental distribution

oxide debris acted as an asperity in the worn surface, and lowered the wear mass loss by reducing the true contact between the cladding layers and counterpart.

### 3.7 Lap Shear Study

The variation of shear bond strength of different cladding layers is depicted in Fig. 20. For shear bond strength, tensile load was applied until the bond failure between cladding and substrate. The shear bond strength between cladding and substrate are found to be decreasing with increasing cladding

thickness. The maximum applied load was found to be 5.8 kN in 1 mm cladding layer, when compared to 3 mm cladding layer at 5.1 kN. The corresponding average bond strengths (load divided by bonding area) are 88 and 77 MPa. The major cause of the failure is attributed to the temperature gradient in the vicinity of cladding and substrate region, which increased the hard and brittle intermetallics in the interface region. Again, the residual stresses around the interfaces can also influence the mechanical behavior of the dissimilar joints. Residual stress at the interface might be affected by resultant compressive

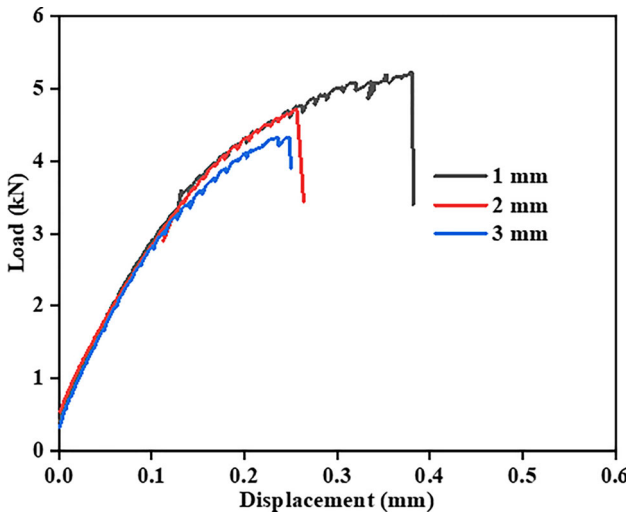


**Fig. 20** Load versus displacement in lap shear test for cladding layers of different thicknesses

residual stress in the coating and the substrate. As the CMT coating is thickened, the residual stresses within the coating increase, causing reduction in the shear bond strength. Moreover, the likelihood of defects forming between deposited layers also increases that directly impacts the bond strength. Factors like longer deposition times or higher temperatures required for thicker layers will enhance defect formation, including voids, cracks, or interfacial discontinuities. These defects act as stress concentrators within the bond interface, reducing effective bonding area and compromising overall strength. Voids can initiate cracks under load; while, interfacial discontinuities can lead to delamination. These aspects will be studied in detail through the finite element method modeling of the process.

## 4. Conclusion

In this work, Fe-based cladding of different layer thicknesses was fabricated on aluminum substrate with cold metal transfer technology. Microstructural, tribological and mechanical properties were obtained in each thickness and compared. The following are the salient observations:

- Among 1, 2 and 3 mm thick cladding layers, the quality of bead in 1 mm thick layer was the best. It had the minimum dilution, reduced porosity, low bead contact angle and relatively smoother surface. The thin cladding layer provided fine grain structure and enhanced low angle grain boundaries. The presence of higher amount such boundaries in 1 mm cladding layer also resulted in the higher dislocation density. In general, this resulted in enhanced mechanical properties like hardness and wear resistance.
- Due to higher cooling rate in 1 mm cladding layer, a martensite structure was obtained that contributed to enhanced hardness. In other layers, the structure was largely ferrite.
- The fine grain, dense martensite phase and higher dislocation density has resulted in high microhardness of 282

HV, low Lancaster wear coefficient of  $0.88 \times 10^{-5}$  mm<sup>3</sup>/Nm and enhanced shear bond strength of 88 MPa in 1 mm thick cladding layer. Corresponding values for 3 mm thick cladding layer were 249 HV and  $1.03 \times 10^{-5}$  mm<sup>3</sup>/Nm; amounting to 12 and 17% deviations, respectively.

Considering these observations, the optimization of layer thickness in cladding as well as additive manufacturing is crucial. In additive manufacturing, a trade-off has to be made between productivity and mechanical properties; low layer thickness provides good mechanical properties but will require more time for fabrication. Developing the physics or database models of the cladding process using CMT will help in the optimization.

## Acknowledgments

The testing facility at the Indian Institute of Technology Guwahati (IITG) was made available by the CIF. The CMT Machine was acquired by the IITG Technology Innovation and Development Foundation, which is a part of NMICPS, under grant number DST/NMICPS/TIH12/IITG/2020. Mr. Abhijeet Dhulekar helped with the experimentation, which is appreciatively acknowledged.

## Author Contributions

Bappa Das contributed to writing the first draft, conceptualization; experimentation, B.N. Panda contributed to supervision; checking the draft, U.S. Dixit contributed to conceptualization, supervision, interpretation of results; technical writing and finalization of the draft.

## Conflict interest

The authors declare that they have no known competing financial interests or personal relationships that could have appeared to influence the work reported in this paper.

## References

- P. Wang, X. Chen, Q. Pan, B. Madigan, and J. Loag, Laser Welding Dissimilar Materials of Aluminum to Steel: An Overview, *Int. J. Adv. Manuf. Technol.*, 2016, **87**, p 3081–3090. <https://doi.org/10.1007/s00170-016-8725-y>
- H.J. Park, S. Rhee, M.J. Kang, and D.C. Kim, Joining of Steel to Aluminum Alloy by AC Pulse MIG Welding, *Mater. Trans.*, 2009, **50**, p 2314–2317. <https://doi.org/10.2320/matertrans.M2009105>
- S. Selvi, A. Vishvaksenan, and E. Rajasekar, Cold Metal Transfer (CMT) Technology: An Overview, *Def. Technol.*, 2018, **14**, p 28–44. <https://doi.org/10.1016/j.dt.2017.08.002>
- J. Feng, H. Zhang, and P. He, The CMT Short-circuiting Metal Transfer Process and its Use in Thin Aluminium Sheets Welding, *Mater. Des.*, 2009, **30**, p 1850–1852. <https://doi.org/10.1016/j.matdes.2008.07.015>
- G. Lorenzin and G. Rutili, The Innovative Use of Low Heat Input In Welding: Experiences on ‘Cladding’ and Brazing Using the CMT Process, *Weld. Int.*, 2009, **23**, p 622–632. <https://doi.org/10.1080/09507110802543252>
- C.G. Pickin, S.W. Williams, and M. Lunt, Characterization of the Cold Metal Transfer (CMT) Process and Its Application for Low Dilution Cladding, *J. Mater. Proc. Technol.*, 2011, **211**, p 496. <https://doi.org/10.1016/j.jmatprotec.2010.11.005>

7. A. Sova, S. Grigoriev, A. Okunkova, and I. Smurov, Cold Spray Deposition of 316L Stainless Steel Coatings on Aluminum Surface with Following Laser Post-Treatment, *Surf. Coating. Technol.*, 2013, **235**, p 283–289. <https://doi.org/10.1016/j.surfoat.2013.07.052>
8. M. Villa, S. Dosta, and J.M. Guilemany, Optimization of 316L Stainless Steel Coatings on Light Alloys using Cold Gas Spray, *Surf. Coating. Technol.*, 2013, **235**, p 220–225. <https://doi.org/10.1016/j.surfoat.2013.07.036>
9. J. Zhou, K. Ma, C.X. Li, M. Yasir, X.T. Luo, and C.J. Li, Microstructures of Aluminum Surfaces Reinforced with 316L Stainless Steel Particles Via High-Speed Particle Injection and the Resulting Double Strengthening Mechanism, *Surf. Coating. Technol.*, 2020, **385**, 125380. <https://doi.org/10.1016/j.surfoat.2020.125380>
10. T. Laha, A. Agarwal, T. McKechnie, K. Rea, and S. Seal, Synthesis of Bulk Nanostructured Aluminum Alloy Component through Vacuum Plasma Spray Technique, *Acta Mater.*, 2005, **53**, p 5429. <https://doi.org/10.1016/j.actamat.2005.08.027>
11. G.P. Rajeev, M. Kamaraj, and R.S. Bakshi, Comparison of Microstructure, Dilution and Wear Behavior of Stellite 21 Hardfacing on H13 Steel Using Cold Metal Transfer and Plasma Transferred Arc Welding Processes, *Surf. Coating. Technol.*, 2019, **375**, p 383–394. <https://doi.org/10.1016/j.surfoat.2019.07.019>
12. B. Das, B.N. Panda, and U.S. Dixit, Microstructure and Mechanical Properties of ER70S-6 Alloy Cladding on Aluminum Using a Cold Metal Transfer Process, *J. Mater. Eng. Perform.*, 2022, **31**, p 9385–9398. <https://doi.org/10.1007/s11665-022-06937-8>
13. B. Das, B.N. Panda, and U.S. Dixit, Corrosion Behavior and Its Effect on Mechanical Properties of ER70S-6 Cladding on AA 6061-T6 Alloy Using a Cold Metal Transfer Process, *Low Cost Manufacturing Technologies*. S.N. Joshi, U.S. Dixit, R.K. Mittal, S. Bag Ed., NERC Springer, Singapore, 2022, p 21–29
14. B. Das, B.N. Panda, and U.S. Dixit, Effects of Heat Treatment on the Mechanical Properties of Fe-Based ER70S-6 Cladding on Aluminum Substrate Using Cold Metal Transfer Process, *J. Mater. Eng. and Perform.*, 2024, **33**, p 173–193. <https://doi.org/10.1007/s11665-023-07975-6>
15. Y. Xiong, W. Zhuang, and M. Zhang, Effect of The Thickness of Cold Sprayed Aluminium Alloy Coating on the Adhesive Bond Strength with an Aluminium Alloy Substrate, *Surf. Coating. Technol.*, 2015, **270**, p 259–265. <https://doi.org/10.1016/j.surfoat.2015.02.048>
16. A. Moridi, S.M.H. Gangaraj, S. Vezzu, and M. Guagliano, Number of Passes and Thickness Effect on Mechanical Characteristics of Cold Spray Coating, *Proced. Eng.*, 2014, **74**, p 449–459. <https://doi.org/10.1016/j.proeng.2014.06.296>
17. D.J. Greving, J.R. Shadley, E.F. Rybicki, D.J. Rybicki, J.R. Greving, and E.F.R. Shadley, Effects of Coating Thickness and Residual Stresses on the Bond Strength of ASTM C633–79 Thermal Spray Coating Test Specimens, *J. Therm. Spray Technol.*, 1994, **3**, p 371–378. <https://doi.org/10.1007/BF02658982>
18. A. Ermakova, A. Mehmankar, S. Ganguly, J. Razavi, and F. Berto, Fatigue Crack Growth Behaviour of Wire and Arc Additively Manufactured ER70S-6 Low Carbon Steel Components, *Int. J. Fract.*, 2021 <https://doi.org/10.1007/s10704-021-00545-8>
19. ER70S-6 – Weld Wire. [http://www.weldwire.net/weld\\_products/w\\_w70s-6/](http://www.weldwire.net/weld_products/w_w70s-6/). Accessed 29 Jan 2024
20. A. Aprilia, W. Zhai, Y. Guo, R.S. Aishwarya, and W. Zhou, Decarburization of Wire-Arc Additively Manufactured ER70S-6 Steel, *Materials.*, 2023, **16**, p 3635. <https://doi.org/10.3390/ma16103635>
21. G.P. Rajeev, M. Kamaraj, and R.S. Bakshi, Al-Si-Mn Alloy Coating on Aluminum Substrate using Cold Metal Transfer (CMT) Welding Technique, *JOM*, 2014, **66**, p 1061–1067. <https://doi.org/10.1007/s11837-014-0970-7>
22. Y. Zhou and Q. Lin, Wetting of Galvanized Steel by Al 4043 Alloys in the First Cycle of CMT Process, *J. Alloy. Compd.*, 2014, **589**, p 307–313. <https://doi.org/10.1016/j.jallcom.2013.11.177>
23. T. Ponomareva, M. Ponomarev, A. Kisarev, and M. Ivanov, Wire Arc Additive Manufacturing of Al-Mg Alloy with the Addition of Scandium and Zirconium, *Mater.*, 2021, **14**, p 3665. <https://doi.org/10.3390/ma14133665>
24. W. Li, K. Sugio, X. Liu, M. Yamamoto, Y. Guo, S. Zhu, and G. Sasaki, Microstructure Evolution and Mechanical Properties of 308L Stainless Steel Coatings Fabricated by Laser Hot Wire Cladding, *Mater. Sci. Eng. A*, 2021, **824**, 141825. <https://doi.org/10.1016/j.msea.2021.141825>
25. P. Guo, B. Zou, C. Huang, and H. Gao, Study on Microstructure, Mechanical Properties and Machinability of Efficiently Additive Manufactured AISI 316L Stainless Steel by High-Power Direct Laser Deposition, *J. Mater. Process. Technol.*, 2017, **240**, p 12–22. <https://doi.org/10.1016/j.jmatprotec.2016.09.005>
26. S.I. Wright, M.M. Nowell, and D.P. Field, A Review of Strain Analysis using Electron Backscatter Diffraction, *Microsc. Microanal.*, 2011, **17**, p 316–329. <https://doi.org/10.1017/S1431927611000055>
27. D.Y. Lin, L.Y. Xu, Y.D. Han, Y.K. Zhang, H.Y. Jing, L. Zhao, and F. Minami, Structure and Mechanical Properties of a Fecocrni High-Entropy Alloy Fabricated via Selective Laser Melting, *Intermetallics*, 2020, **127**, p 106963. <https://doi.org/10.1016/j.intermet.2020.106963>
28. J. Huang, W.P. Li, J.Y. He, R. Zhou, T. Chou, T. Yang, C.T. Liu, W.D. Zhang, Y. Liu, and J.C. Huang, Dual Heterogeneous Structure Facilitating an Excellent Strength-Ductility Combination in an Additively Manufactured Multi-Principal-Element Alloy, *Mater. Res. Lett.*, 2022, **10**, p 575–584. <https://doi.org/10.1080/21663831.2022.2067790>
29. M. Mohammadnezhad, V. Javaheri, M. Shamanian, S. Rizaneh, and J. Szpunar, Insight to the Microstructure Characterization of a HP Austenitic Heat Resistant Steel after Long-term Service Exposure, *Acta Metall. Slovaca.*, 2018, **24**, p 296. <https://doi.org/10.12776/ams.v24i4.1160>
30. S. Mohan Kumar, A. Rajesh Kannan, N. Pravin Kumar, R. Pramod, N. Siva Shammugam, A.S. Vishnu, and S.G. Channabasavanna, Microstructural Features and Mechanical Integrity of Wire Arc Additive Manufactured SS321/Inconel 625 Functionally Gradient Material, *J. Mater. Eng. and Perform.*, 2021, **30**, p 5692–5703. <https://doi.org/10.1007/s11665-021-05617-3>
31. P. Li, S. Chen, H. Dong, H. Ji, Y. Li, X. Guo, G. Yang, X. Zhang, and X. Han, Interfacial Microstructure and Mechanical Properties of Dissimilar Aluminum/Steel Joint Fabricated via Refilled Friction Stir Spot Welding, *J. Manuf. Process.*, 2020, **49**, p 385–396. <https://doi.org/10.1016/j.jmapro.2019.09.047>
32. E. Fereiduni, M. Movahedi, and A.H. Kokabi, Aluminum/Steel Joints Made by an Alternative Friction Stir Spot Welding Process, *J. Mater. Process. Technol.*, 2015, **224**, p 1–10. <https://doi.org/10.1016/j.jmatprotec.2015.04.028>
33. H. Sina, J. Corneliusson, K. Turba, and S. Iyengar, A Study on the Formation of Iron Aluminide (Feal) from Elemental Powders, *J. Alloys Compd.*, 2015, **636**, p 261–269. <https://doi.org/10.1016/j.jallcom.2015.02.132>
34. Y. Ju, A. Goodall, M. Strangwood, and C. Davis, Characterisation of Precipitation and Carbide Coarsening in Low Carbon Low Alloy Q&T Steels During the Early Stages of Tempering, *Mater. Sci. Eng. A*, 2018, **738**, p 174–189. <https://doi.org/10.1016/j.msea.2018.09.044>
35. K. Chen, Z. Jiang, F. Liu, H. Li, X. Ma, B. Zhao, C. Kang, and Y. Li, Enhanced Mechanical Properties by Retained Austenite in Medium-Carbon Si-Rich Microalloyed Steel Treated by Quenching-Tempering, Austempering and Austempering-Tempering Processes, *Mater. Sci. Eng. A*, 2020, **790**, p 39742. <https://doi.org/10.1016/j.msea.2020.139742>
36. P. Zhang, Y. Chen, W. Xiao, D. Ping, and X. Zhao, Twin Structure of the Lath Martensite in Low Carbon Steel, *Prog Nat Sci Mater Int.*, 2016, **26**, p 169–172. <https://doi.org/10.1016/j.pnsc.2016.03.004>
37. J. Wang, X. Cui, G. Jin, Y. Zhao, X. Wen, and Y. Zhang, Effect of In-Situ Ni Interlayer on the Microstructure and Corrosion Resistance of Underwater Wet 316L Stainless Steel Laser Cladding Layer, *Surf. Coating. Technol.*, 2023, **458**, 129341. <https://doi.org/10.1016/j.surfoat.2023.129341>
38. S. Tardio, M.L. Abel, R.H. Carr, J.E. Castle, and J.F. Watts, Comparative Study of the Native Oxide on 316L Stainless Steel by XPS and ToF-SIMS, *J. Vac. Sci. Technol. A*, 2015, **33**, p 05E122. <https://doi.org/10.1116/1.4927319>
39. X. Chen, Y. Li, Y. Zhu, Y. Bai, and B. Yang, Improved Corrosion Resistance of 316LN Stainless Steel Performed by Rotationally Accelerated Shot Peening, *Appl. Surf. Sci.*, 2019, **481**, p 1305–1312. <https://doi.org/10.1016/j.apsusc.2019.03.256>
40. S.H.M. Anijdan, M. Sabzi, M. Ghobeiti-Hasab, and A. Roshan-Ghiyas, Optimization of Spot-Welding Process Parameters in Dissimilar Joint of Dual Phase Steel DP600 and AISI 304 Stainless Steel to Achieve the Highest Level of Shear-Tensile Strength, *Mater. Sci. Eng. A*, 2018, **726**, p 120–125. <https://doi.org/10.1016/j.msea.2018.04.072>
41. E.O. Hall, The Deformation and Ageing of Mild Steel: III Discussion of Results, *Proc. Phys. Soc. Series B*, 1951, **64**, p 747–753

42. N.J. Petch, The Cleavage Strength of Polycrystals, *J. Iron Steel Inst.*, 1953, **174**, p 25–28
43. D. Das, A.K. Dutta, V. Toppo, and K.K. Ray, Effect of Deep Cryogenic Treatment on the Carbide Precipitation and Tribological Behavior of D2 Steel, *Mater. Manuf. Process.*, 2007, **22**, p 474–480. <https://doi.org/10.1080/10426910701235934>
44. M. Ali, D. Porter, J. Kömi, M. Eissa, H.E. Faramawy, and T. Mattar, Effect of Cooling Rate and Composition On Microstructure and Mechanical Properties of Ultrahigh-Strength Steels, *J. Iron. Steel Res. Int.*, 2019, **26**, p 1350–1365. <https://doi.org/10.1007/s42243-019-00276-0>
45. J. Archard, Contact and Rubbing of Flat Surfaces, *J. Appl. Phys.*, 1953, **24**, p 981–988. <https://doi.org/10.1063/1.1721448>
46. J. Denape and J. Lamon, Sliding Friction of Ceramics: Mechanical Action of the Wear Debris, *J. Mater. Sci.*, 1990, **25**, p 3592–3604. <https://doi.org/10.1007/BF00575394>
47. J.K. Lancaster, The Influence of Substrate Hardness on the Formation and Endurance of Molybdenum Disulphide Films, *Wear*, 1967, **10**, p 103–117. [https://doi.org/10.1016/0043-1648\(67\)90082-8](https://doi.org/10.1016/0043-1648(67)90082-8)
48. M. Qunshuang, L. Yajiang, W. Juan, and L. Kun, Microstructure Evolution and Growth Control of Ceramic Particles in Wide-Band
- Laser Clad Ni60/WC Composite Coatings, *Mater. Des.*, 2016, **92**, p 897–905
49. C. Wen-Ruey, H. Mikko, and G. Raoul, The effects of Cut-off Length on Surface Roughness Parameters and their Correlation with Transition Friction, *Saf. Sci.*, 2004, **42**, p 755–769. <https://doi.org/10.1016/j.ssci.2004.01.002>
50. Z. Peng and T.B. Kirk, Computer Image Analysis of Wear Particles in Three-dimensions for Machine Condition Monitoring, *Wear*, 1998, **223**, p 157–166. [https://doi.org/10.1016/S0043-1648\(98\)00280-4](https://doi.org/10.1016/S0043-1648(98)00280-4)

**Publisher's Note** Springer Nature remains neutral with regard to jurisdictional claims in published maps and institutional affiliations.

Springer Nature or its licensor (e.g. a society or other partner) holds exclusive rights to this article under a publishing agreement with the author(s) or other rightsholder(s); author self-archiving of the accepted manuscript version of this article is solely governed by the terms of such publishing agreement and applicable law.